Separation and Purification Technology 423 (2027) 140716

Contents lists available at ScienceDirect

Separation and Purification Technology

journal homepage: www.elsevier.com/locate/seppur

Continuous Electroreduction of Cr(VI) in a flow-through system based on mesoporous carbon monolith with high efficiency: influence of power supply modes

Tairan Zhang [a,b], Jiangnan Huang [a,*], Hongjuan Wang [b], Hao-Fan Wang [b], Hao Yu [b], Yonghai Cao [b,*]

[a] College of Chemistry and Chemical Engineering, Zhongkai University of Agriculture and Engineering, Guangzhou, 510550, China
[b] School of Chemistry and Chemical Engineering, Guangdong Provincial KeyLab of Green Chemical Product Technology, South China University of Technology, Guangzhou, 510641, China

ARTICLE INFO

Editor name: Prof. Yan Zhao

Keywords:
Flow-through electrode
Cr(VI) reduction
Electrochemical water treatment
Electron flux matching
Mass transfer
Mesoporous carbon

ABSTRACT

The performance of flow-through electrode systems (FES) for water treatment is often limited by the mismatch between the external driving mode and the material properties of the porous electrodes. In this study, a continuous-flow FES based on mesoporous carbon monolith (o-MCM) was developed to investigate the interactions among mass transfer, interfacial kinetics, and operational modes during Cr(VI) electro-reduction. A superior Cr(VI) removal efficiency (> 99%) coupled with low specific energy consumption (SEC, from 140 to 250 Wh mol^{-1}) and high electron efficiency (EE) over the optimized o-MCM-900 electrode was obtained. Using an anode-cathode cross-swap method, the dominant operational constraints under different driving modes were elucidated: the constant voltage (CV) mode is largely constrained by overall Ohmic/cell resistance, while the constant current (CC) mode is predominantly governed by interfacial activation kinetics. To address mass transfer limitations at high flow rates, a dynamic load-responsive electron flux matching CC strategy was proposed. Through dynamic polarization regulation, this strategy effectively counteracted the mass-transfer resistance encountered under low Damköhler number conditions ($Da < 3$), maintaining high Cr(VI) removal (> 99%) and high EE (> 99%) even at a short residence time of 3.49 s (15 mL min^{-1}). Moreover, the hydrodynamic shear forces within the pore channels prevented Cr(III) passivation, ensuring stable operation for over 400 min with considerable activity. This work provides practical reaction engineering guidelines for matching material properties with operating strategies in flow-through electrochemical systems.

1. Introduction

Owing to the severe toxicity and high environmental mobility, the removal of hexavalent chromium (Cr(VI)) from industrial effluents remains a persistent environmental challenge [1–5]. Recently, electrochemical and catalytic oxidation/reduction technologies have attracted significant attention for wastewater treatment [6–8]. Electrochemical reduction has emerged as a promising technology due to its chemical-free nature and ease of continuous operation, fundamentally relying on cathodic electron transfer to convert toxic Cr(VI) into less harmful Cr (III) [9–11]. To enhance this interfacial conversion, the flow-through electrode systems (FES) configured with porous materials have been widely adopted [12–16]. By forcing the electrolyte directly through hierarchical porous materials, FES significantly compresses the diffusion boundary layer and alleviates the mass transfer limitations. To further optimize performance, various spatial configurations and temporal electric field modulations were explored [16]. For instance, researchers have designed specific sequential anode-cathode configurations for in-situ proton generation, and utilized alternating voltage strategies to decouple electrostatic adsorption and faradaic reduction, thereby suppressing parasitic reactions and improving energy efficiency [10,17,18].

Despite these hydrodynamic and configurational advancements, the optimization of FES faces a critical, yet frequently overlooked, scientific problem: the intrinsic mismatch between external operational modes and the physicochemical properties of porous electrodes. The operational mode, primarily potentiostatic (constant voltage, CV) or

* Corresponding authors.
E-mail addresses: huangjiangnan@zhku.edu.cn (J. Huang), meyhcao@scut.edu.cn (Y. Cao).

https://doi.org/10.1016/j.seppur.2026.140716
Received 31 July 2026; Received in revised form 24 October 2026; Accepted 26 October 2026
Available online 27 October 2026
1383-5866/© 2026 Elsevier B.V. All rights are reserved, including those for text and data mining, AI training, and similar technologies.

galvanostatic (constant current, CC), dictates the polarization distribution and key factors within the porous matrix [19,20]. Under the CV mode, the system often suffers from apparent Ohmic voltage drops along the electrode depth [21]. This causes the local overpotential to decay rapidly, confining faradaic reactions to the outer surface and leaving internal sites underutilized (i.e., operating in an Ohmic-controlled regime). Conversely, CC operation forces a predetermined electron flux, extending polarization deeper into the matrix [22]. However, it elevates the risk of excessive local overpotentials, which can initiate parasitic reactions such as hydrogen evolution reaction (HER) if the interfacial kinetics cannot accommodate the forced current (i.e., operating in a kinetic-controlled regime). Currently, the development of nanostructured catalysts relies on trial-and-error approaches aimed at boosting apparent current densities. A mechanistic decoupling of how specific material features such as bulk electrical conductivity versus surface active sites match the distinct polarization constraints of the CV and CC modes remains unaddressed.

To bridge this gap, the electro-reduction of Cr(VI) serves as an ideal probe reaction, as its complex proton-coupled electron transfer (PCET) nature is sensitive to both the electron transport network and the availability of surface proton-donor sites [23,24]. In this study, we established a system-level reaction engineering framework to decouple the transport and interfacial kinetic mechanisms in FES. Mesoporous carbon monolith (MCM) electrodes with gradient physicochemical properties were synthesized by precisely tuning the carbonization temperature (regulating bulk conductivity) and subsequent oxidative treatments (regulating surface active groups). By comprehensively evaluating the FES performance under varying hydrodynamic conditions and electrical modes, combined with systematic electrochemical impedance spectroscopy and an innovative cross-electrode configuration experiment, we quantitatively mapped the shift in the CV/CC mode. Our findings demonstrate that the CV mode is constrained by Ohmic resistance, demanding high bulk conductivity, whereas the CC mode operates under a kinetic-controlled regime that heavily depends on surface active sites. It should be noted that our previous efforts have explored the use of MCM for Cr(VI) remediation via non-faradaic electrostatic adsorption under weak electric fields [25], and demonstrated the transition to electro-reduction by modifying macroscopic reactor configurations [26]. However, the fundamental transport-kinetic interplay governing this continuous faradaic conversion remains unresolved. Distinct from focusing on material adsorptive capacity or empirical reactor design, the present study represents a conceptual shift toward fundamental chemical reaction engineering. Herein, we aim to fundamentally decouple the intricate interplay between mass-transfer limitations and interfacial activation kinetics under distinct operational polarization modes (CV vs. CC).

2. Experimental section

2.1. Synthesis of MCM materials

The MCM was synthesized via a soft-templating and self-assembly method [25,27]. Initially, 45.0 g of resorcinol and 18.75 g of Pluronic F127 triblock copolymer ($PEO_{106}PPO_{70}PEO_{106}$) were dissolved in a mixed solvent containing 171 mL of absolute ethanol and 135 mL of deionized water. The mixture was stirred continuously at room temperature for 15 min until complete dissolution was achieved. Subsequently, 1.165 g of hexamethylenediamine was added to the solution, followed by stirring for 45 min to ensure homogeneous mixing. Formaldehyde solution (61.6 mL, 37 wt%) was then added dropwise. After continuous stirring for approximately 20 min, the solution turned milky white, indicating the successful formation of the MCM precursor.

The precursor solution was cast into cylindrical molds and subjected to a multi-stage curing process in an oven: initially dried at 50 °C for 24 h, transferred to 60 °C for another 24 h, and finally cured at 100 °C for 12 h. This step-wise temperature programming (50 °C, 60 °C, and 100 °C) was applied to control the condensation rate of the resorcinol-formaldehyde resin [28]. Direct curing at 100 °C causes rapid solvent vaporization and high internal stress, which fractures the initial gel. The mild 50–60 °C stages allow uniform polycondensation and gentle solvent evaporation to build a robust skeleton, while the 100 °C stage ensures deep cross-linking. The solidified polymer monoliths were then placed in a tubular furnace and carbonized under a nitrogen atmosphere. The temperature was ramped at a heating rate of 2 °C min^{-1} to the target temperature and maintained for 2 h to yield the unmodified MCM materials. To enhance the surface hydrophilicity and introduce oxygen-containing functional groups, the carbonized MCM materials were immersed in 100 mL of H_2O_2 aqueous solution (3 wt%) and treated with ultrasonication for 60 min. The resulting oxidized materials were denoted as o-MCM-X, where "o" represents the oxidative modification and "X" denotes the carbonization temperature (e.g., 800, 900, 1000, 1100 °C). For comparative studies, the pristine carbon material carbonized at 900 °C without H_2O_2 treatment was labeled as MCM-900.

2.2. Electrochemical reduction of Cr(VI)

The continuous-flow electro-reduction of Cr(VI) was conducted in a custom-designed dual-chamber electrochemical cell, as illustrated in Fig. 1. The typical monolithic carbon electrode (diameter: 1.65 cm, thickness: 0.48 cm, geometric volume: 1.026 cm^3, and mass: 0.31 g) was mounted between the chambers. The flow channel connecting the chambers had a diameter of 1.0 cm and a length of 0.5 cm. The Cr(VI)-containing electrolyte was continuously pumped through the reactor from the bottom to the top using a peristaltic pump.

The effluent was periodically sampled at the reactor outlet to determine the concentrations of Cr(VI) and total dissolved chromium. Cr (VI) concentration was quantified using the 1,5-diphenylcarbazide colorimetric method via a UV–vis spectrophotometer (UV-2450, Shimadzu). The total chromium concentration was measured using an atomic absorption spectrophotometer (AAS, Z-2000, Hitachi). The concentration of generated Cr(III) in the effluent was calculated by subtracting the Cr(VI) concentration from the total chromium concentration (**Eq. 1**). All liquid-phase concentration measurements (Cr(VI) and total Cr ions) were conducted in triplicate ($n = 3$) to minimize instrumental and analytical errors. The removal efficiency ($X_{Cr(VI)}$) and the reduction ratio (R) for Cr(VI) ions were calculated according to **Eqs. 2–3**:

$$C_{t,\,Cr(III)} = C_{t,\,Total} - C_{t,\,Cr(VI)} \quad (1)$$

$$X_{Cr(VI)} = (C_{0,\,Cr(VI)} - C_{t,\,Cr(VI)})/C_{0,\,Cr(VI)} \times 100\% \quad (2)$$

$$R = C_{t,\,Cr(III)} \,/\, (C_{0,\,Cr(VI)} - C_{t,\,Cr(VI)}) \times 100\% \quad (3)$$

where $C_{0,Cr(VI)}$ is the initial influent Cr(VI) concentration (mg L^{-1}), and $C_{t,Cr(VI)}$, $C_{t,Total}$, and $C_{t,Cr(III)}$ represent the concentrations (mg L^{-1}) of Cr (VI), total Cr ions (AAS detected), and Cr(III) ions in the effluent at sampling time t, respectively. A higher value of R indicates that the Cr (VI) removal process is predominantly driven by electrochemical reduction to soluble Cr(III) rather than physical adsorption or surface precipitation.

To evaluate the engineering economic feasibility, the specific energy consumption (SEC, Wh mol^{-1}) under CV and CC modes was determined by **Eqs. 4** and **5**, respectively:

$$SEC_{CV} = 1000MU \int_{t1}^{t2} I(t)dt \Big/ Q \int_{t1}^{t2} \left(C_{0,Cr(VI)} - C_{t,Cr(VI)}(t)\right) dt \quad (4)$$

$$SEC_{CC} = 1000MI \int_{t1}^{t2} U(t)dt \Big/ Q \int_{t1}^{t2} \left(C_{0,Cr(VI)} - C_{t,Cr(VI)}(t)\right) dt \quad (5)$$

where M is the molar mass of chromium (52.00 g mol^{-1}), U is the applied voltage (V) in CV mode, and I(t) is the corresponding instantaneous current response (A). Conversely, I is the applied current (A) in CC

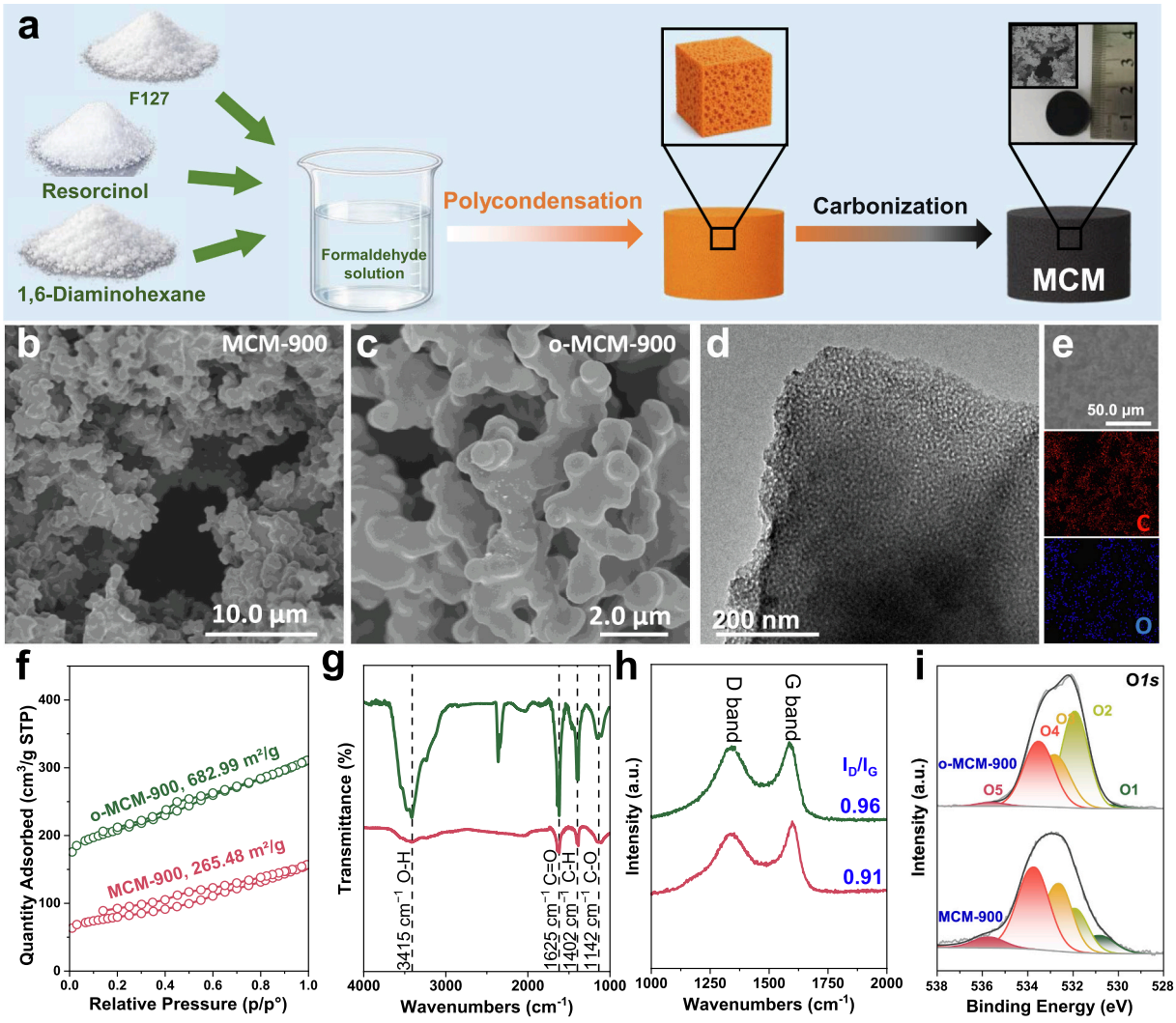

Fig. 1. (a) Schematic illustration of the synthesis process of the carbon materials. SEM images of MCM-900 (b) and o-MCM-900 (c). TEM image (d) and EDS mapping (e) of o-MCM. N_2 adsorption-desorption isotherms (f), Raman spectra (g), FTIR spectra (h), and high-resolution O 1 s XPS spectra (i) of the materials.

mode, and U (t) is the corresponding instantaneous applied voltage (V). Q denotes the volumetric flow rate (Lh^{-1}), and the integral bounds from t_1 to t_2 represent the evaluated operational time interval (h).

Furthermore, the theoretical current required for the reduction of Cr (VI), denoted as $I_{\text{Theory, red}}$ (A), can be determined based on Faraday's law of electrolysis according to **Eq. 6**:

$$I_{Theory.red} = \frac{z \bullet F \bullet Q \bullet C_0 \bullet X_{rem} \bullet R_{red}}{3600 \bullet 1000 \bullet M} \tag{6}$$

Consequently, the overall electron efficiency (EE, %) of the FES process is calculated as the ratio of the theoretical current requirement to the actual applied current, as expressed in **Eq. 7**:

$$EE(\%) = \frac{I_{Theory.red}}{I_{Actual}} \times 100\% = \frac{z \bullet F \bullet Q \bullet C_0 \bullet X_{rem} \bullet R_{red}}{3600 \bullet 1000 \bullet M \bullet I_{Actual}} \times 100\% \tag{7}$$

where z is the number of electrons transferred per ion during the faradaic reaction ($z = 3$ for the reduction of Cr(VI) to Cr(III)). F represents the Faraday constant (96,485C mol^{-1}). Q signifies the volumetric flow rate of the electrolyte (L h^{-1}). C_0 is the initial mass concentration of Cr (VI) in the influent (mg L^{-1}). M is the molar mass of chromium (52.00 g mol^{-1}). The parameters X_{rem} and R_{red} denote the Cr(VI) removal efficiency and the faradaic reduction ratio (i.e., the proportion of the removed Cr(VI) that is actually reduced to Cr(III)), respectively. Physically, $I_{\text{Theory, red}}$ represents the absolute minimum current required to achieve the observed amount of Cr(VI) reduction under ideal conditions, assuming that 100% of the supplied electrons are utilized for the target PCET reaction without any parasitic side reactions or energetic losses. I_{Actual} (A) refers to the actual instantaneous or constant current passed through the reactor during the experiment, which was directly recorded by the electrochemical workstation.

Substituting these parameters into **Eqs. 4** or **5** yields **Eq. 8**:

$$\text{SEC} = \text{U} \times \left(\frac{zF}{EE}\right) \tag{8}$$

2.3. Calculation of hydraulic residence time (τ) and Damköhler number (*Da*)

In a flow-through porous electrode, assuming a mass-transport-controlled regime where interfacial charge transfer is instantaneous, the local pollutant concentration at the electrode surface approaches zero ($C_s \approx 0$). The fluid dynamics can be modeled as a one-dimensional plug flow reactor (PFR) [29,30]. To decouple the hydrodynamics from interfacial mass transfer, the actual τ at various volumetric flow rates (Q) was calculated based on the porosity (ε) of the carbon electrode (**Eq. 9**):

$$\tau = (V_{\text{Bulk}} \times \varepsilon)/Q \tag{9}$$

Where V_{Bulk} is the geometric bulk volume of the electrode (cm^3) and

Q is the volumetric flow rate (mL min^{-1}). The ε was determined from the ratio of the apparent bulk density (ρ_{Bulk}) to the skeletal density ($\rho_{Skeleton}$, approximately 2.01 g cm^{-3}) (**Eq. 10**):

$$\varepsilon = \left(1 - \rho_{Bulk/}\rho_{Skeleton}\right) \times 100\% \quad (10)$$

For a differential volume element (dV) within the PFR, the steady-state mass balance equation is formulated as follows (**Eq. 11**):

$$Q{\cdot}dC = -k_m{\cdot}a_e{\cdot}(C - C_S){\cdot}dV \quad (11)$$

Given that $C_S \approx 0$ and $dV/Q = d\tau$ (representing the differential hydraulic residence time), the above equation simplifies to (**Eq. 12**):

$$\frac{dC}{C} = -k_m{\cdot}a_e{\cdot}d\tau \quad (12)$$

Integrating Eq. 12 from the reactor inlet ($\tau = 0$, $C = C_{in}$) to the outlet ($\tau = \tau_{total}$, $C = C_{out}$) yields **Eq. 13**:

$$\ln\left(\frac{C_{out}}{C_{in}}\right) = -k_m{\cdot}a_e{\cdot}\tau \quad (13)$$

Rearranging this exponential relationship gives (Eq. 14).

$$\frac{C_{out}}{C_{in}} = \exp.(-k_m{\cdot}a_e{\cdot}\tau) \quad (14)$$

where k_m is the convective mass transfer coefficient. The removal efficiency of Cr(VI) of the pollutant is defined as (**Eq. 15**):

$$X = \frac{C_{in} - C_{out}}{C_{in}} = 1 - \frac{C_{out}}{C_{in}} \quad (15)$$

Furthermore, the dimensionless Da, defined as the ratio of the fluid residence time to the characteristic mass-transfer time, is expressed as (**Eq. 16**):

$$Da = k_m{\cdot}a_e{\cdot}\tau \quad (16)$$

By substituting **Eqs. 15–16** into **Eq. 14**, the final correlation linking the conversion to the dimensionless parameter is established (**Eqs. 17 and 18**):

$$1\text{-}X = \exp.(\text{-}Da) \quad (17)$$

$$Da = -\ln(1\text{-}X) \quad (18)$$

3. Results and discussions

3.1. Morphology and physicochemical characterizations

In this study, the typical synthesis of monolithic mesoporous carbon (MCM-900) integrated the self-assembly and polycondensation of a phenolic resin precursor, followed by a high-temperature carbonization process (Fig. 1a) [25]. Subsequently, a mild H_2O_2 oxidation treatment was employed to prepare the o-MCM-900 electrode. For a FES system, the cross-scale hierarchical pore structure and interfacial chemical properties dictate the internal fluid dynamics and mass transfer efficiency. The morphologies of the carbon materials were characterized using scanning electron microscopy (SEM). As shown in **Fig. 1b** and **c**, both the MCM-900 and the o-MCM-900 exhibit a 3D continuous macroporous network constructed by highly cross-linked carbon nanoparticles. This micrometer-scale open pore structure is vital, as it not only serves as a low-resistance fluid channel to significantly reduce the pressure drop during reactor operation but also provides an efficient mass transfer pathway for the forced convection of substrates. Transmission electron microscopy (TEM, Fig. 1d) further confirms the dense distribution of highly ordered mesopores within the cross-linked carbon skeleton. Notably, a comparison of the morphological evolution reveals that the H_2O_2 oxidation treatment did not induce the collapse of pore walls or the pulverization of the carbon skeleton, indicating the excellent mechanical stability of the monolithic material [25]. Energy-dispersive X-ray spectroscopy (EDS) mapping illustrates a uniform distribution of oxygen elements across the oxidized carbon matrix (Fig. 1e).

Nitrogen adsorption-desorption analysis shows that the monolithic carbon materials exhibit a typical Type IV isotherm with an H1-type hysteresis loop (Fig. 1f), confirming a mesopore-dominated pore size distribution. Following the oxidation treatment, the specific surface area of o-MCM-900 significantly increased from 265.48 m^2 g^{-1} (for MCM-900) to 682.99 m^2 g^{-1}. This substantial enhancement suggests that the oxidation process effectively removed residual amorphous carbon trapped within the pores, thereby unblocking the micro-scale mass transfer channels and providing more abundant solid-liquid interfaces for the subsequent PCET reactions [31–33]. Raman spectroscopy demonstrates that the defect degree (I_D/I_G ratio) slightly increased from 0.91 for MCM-900 to 0.96 for o-MCM-900 (Fig. 1g). This marginal increment confirms that the oxidation strategy successfully introduced a moderate amount of topological defects (catalytic active centers) onto the carbon basal planes while preserving the continuous sp^2-conjugated conductive carbon skeleton essential for electron transport [34,35]. Fourier transform infrared (FTIR) spectra reveal that, compared to MCM-900, o-MCM-900 displays sharper and more intense characteristic absorption bands at approximately 3400 cm^{-1} (O—H stretching), 1600–1700 cm^{-1} (C═O stretching), and 1100–1200 cm^{-1} (C—O stretching) (Fig. 1h) [25,27], indicating the effective introduction of oxygen-containing functional groups. Further quantitative analysis by XPS reveals that the total surface oxygen content increased from 5.32 at.% to 16.59 at.% post-oxidation (**Fig. S1** and **Table S1**), confirming the efficacy of the oxidative modification. Deconvolution of the high-resolution O 1 s spectra identified five distinct components: carbonyl/quinone oxygen (O1, 530.9 eV), carboxyl oxygen (O2, 531.8 eV), ether linkages (O3, C–O–C, 532.7 eV), hydroxyl groups (O4, –OH, 533.6 eV), and adsorbed oxygen/water (O5, 535.7 eV) (Fig. 1i and **Table S2**) [36–38]. This quantitative analysis indicated a significant increase in the relative proportions of carboxyl (O2, from 20.23% to 34.61%) and ether groups (O3, from 26.31% to 32.91%) after the oxidation treatment. These enriched oxygen-containing functionalities, particularly the carboxyl species, can act as effective proton donors and intermediate bridges to facilitate subsequent interfacial electron transfer [39,40]. These changes in specific surface area and surface oxygen functional groups resulted in a marked enhancement in the interfacial wettability of the materials. Water contact angle measurements verify that the MCM-900 surface exhibits a highly hydrophobic nature with a static contact angle of 134.6° (**Fig. S2**). In contrast, the oxidized o-MCM-900 displays a strong affinity for the aqueous phase; droplets rapidly penetrated the porous channels, reducing the contact angle to approximately 12.8° (approaching a superhydrophilic state). This enhanced hydrophilicity effectively promotes the deep diffusion of water within the porous matrix, suppressing localized channeling effects caused by hydrophobic repulsion, and thereby intensifying the intra-pore mass transfer efficiency.

3.2. Activity in the CV mode

The reaction performance of the FES highly depends on the synergy between the intrinsic properties of the electrode and the hydrodynamic microenvironment within the reactor [12,16]. As illustrated in Fig. 2a, a continuous-flow electrochemical device was constructed to process Cr (VI) ions via a flow-through electro-reduction strategy. The influent was pumped sequentially through the anode and the cathode in a single-pass operation. The impact of the material properties on the treatment performance was first evaluated (Fig. 2b). During the initial stage (< 10 min), the system employing the surface-oxidized o-MCM-900 electrode achieved a Cr(VI) removal efficiency approaching 100%, and this high performance was maintained stably thereafter. In contrast, the removal efficiency of the MCM-900 electrode exhibited rapid

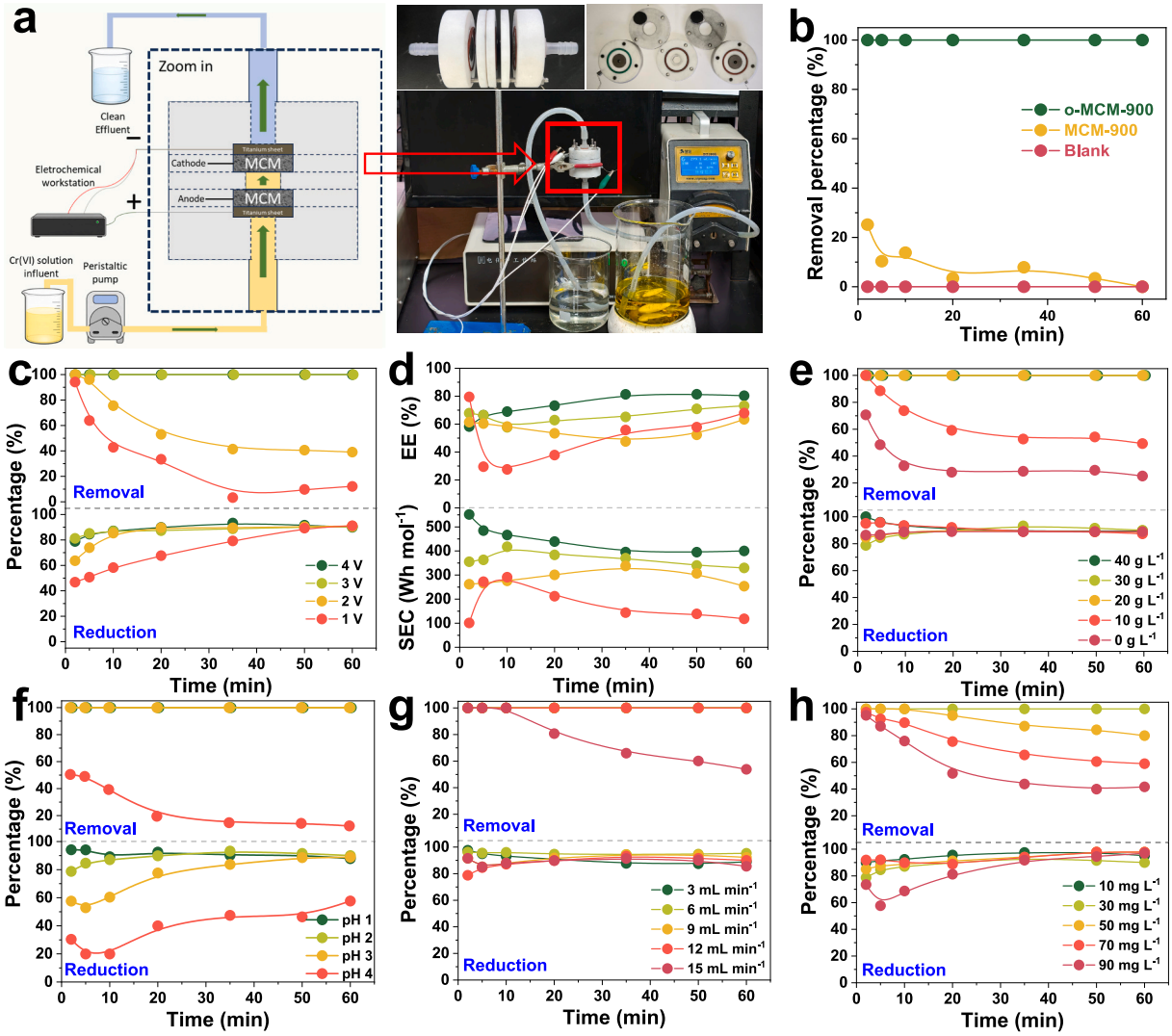

Fig. 2. (a) Schematic illustration and digital photographs of the continuous-flow flow-through electrochemical reactor. (b) Comparison of Cr(VI) removal performance using different cathode materials. (c-h) Effects of various operating parameters on the electro-reduction performance under the CV mode: Time-dependent evolution of removal efficiency and intrinsic reduction ratio under different applied voltages(c) with the corresponding evolution of EE and SEC under varied applied voltages (d), (e) supporting electrolyte concentrations, (f) initial pH values, (g) volumetric flow rates, and (h) initial Cr(VI) concentrations.

breakthrough, dropping to below 10% (the blank control showed negligible removal). Electrochemical characterizations were conducted to elucidate this discrepancy. Cyclic voltammetry scans in the non-Faradaic region revealed that o-MCM-900 possessed a significantly higher specific capacitance (0.58 F g^{-1}) than MCM-900 (0.35 F g^{-1}) (**Fig. S3a** and **Table S3**). This result indicated that the oxidative modification not only introduced polar functional groups onto the carbon skeleton but also conferred a superhydrophilic nature to the surface. This allowed the electrolyte to deeply penetrate the mesoporous network, thereby enhancing the accessibility of Cr(VI) to the interior active sites (i.e., providing a larger electrochemically active surface area, ECSA). Furthermore, the Nyquist plots from electrochemical impedance spectroscopy (EIS) revealed differences in the interfacial transfer mechanisms (**Fig. S3b**). In the high-frequency region, both electrodes exhibited highly comparable bulk Ohmic resistances ($R_s \approx 3.0–3.1\ \Omega$). However, the charge transfer resistance (R_{ct}) of o-MCM-900 (3.3 Ω) was notably lower than that of the untreated MCM-900 (4.6 Ω), demonstrating that the incorporation of oxygen-containing sites effectively lowered the activation energy barrier for the target reduction reaction. Concurrently, o-MCM-900 exhibited a steeper Warburg impedance tail in the low-frequency region, corroborating superior ion diffusion characteristics within the hydrophilic channels [41]. Based on these findings, o-MCM-900 was selected as the electrocatalyst for subsequent investigations.

Under the CV operational mode, the spatial voltage partitioning within the porous reactor must overcome the liquid-phase Ohmic resistance (IR_{cell} drop) and directly dictates the interfacial activation overpotential (η_{act}) driving the electron transfer [42–44]. As shown in Fig. 2c, under a low applied voltage of 1 V, the system exhibited a high apparent removal efficiency within the first 2 min. However, this was primarily attributed to electric double-layer charging and transient physical adsorption on the high-surface-area carbon skeleton. As the polar sites rapidly saturated, the removal efficiency decreased to approximately 10% due to insufficient η_{act} to drive sustained interfacial charge transfer. When the applied voltage was incrementally increased to 3 V and 4 V, the effective overpotential provided by the system successfully overcame the energy barrier for Cr(VI) reduction. This achieved a highly efficient, continuous removal of >99% for a 30 mg L^{-1} influent, with the intrinsic reduction ratio consistently maintained above 90%. The decoupling of the system's energy consumption metrics showed that both EE and SEC increased with the applied voltage (Fig. 2d). Under the high polarization of 4 V, the EE of the system

steadily climbed and stabilized at a high level of approximately 80%. This suggested that a sufficient η_{act} thoroughly activated the interfacial electron transfer, allowing the injected electrons to be efficiently and specifically utilized for the targeted degradation, thereby effectively suppressing parasitic side reactions. However, although high voltage yielded optimal kinetic rates and faradaic selectivity (EE), it incurred higher energy costs. Since SEC is directly proportional to the ratio of voltage to EE (SEC∝U/EE, **Eq. 8**), the multifold increase in the driving potential from 1 V to 4 V substantially outweighed the energy-saving benefits brought by the EE improvement (from ~60% to 80%). Consequently, the SEC under the 4 V condition rose to the range of 350–450 Wh mol^{-1}. Although the 1 V condition yielded a low SEC of 100–150 Wh mol^{-1}, its exceptionally low detoxification throughput (removal percentage < 10%) rendered it impractical for environmental applications.

The effective distribution of voltage across the reactor heavily relies on the modulation of interfacial resistance by the supporting electrolyte. As shown in Fig. 2e, in a pure water system without electrolyte (0 g L^{-1} Na_2SO_4), the externally applied voltage was almost entirely consumed to overcome the bulk liquid resistance and dissipated as ineffective Joule heating. Although an initial removal of ~70% was achieved via capacitive adsorption, it precipitously decayed to below 25%. As the electrolyte concentration was increased to 30 g L^{-1}, the liquid-phase conductivity improved significantly. Under this condition, the removal efficiency was maintained at >99%, the EE peaked (~80%), and the SEC stabilized at 350–400 Wh mol^{-1} (**Fig. S4**). However, when the concentration was overloaded to 40 g L^{-1}, the excessively high ionic strength led to a decrease in the mean activity coefficient according to the Debye-Hückel theory [45], potentially inducing additional faradaic side reactions. Consequently, the SEC of the system rebounded to approximately 500 Wh mol^{-1}.

The solution pH directly dictates the reaction pathway and interfacial proton supply for PCET (Fig. 2f). In a strongly acidic environment (pH = 1), Cr(VI) exists predominantly as the $HCrO_4^-$ species [46,47]. This species exhibits strong oxidizing properties under highly acidic conditions, resulting in a high consistency between the Cr(VI) removal efficiency and the intrinsic reduction ratio (> 99%) throughout the operational cycle. At this state, the EE approached 100%, and the SEC was maintained at a baseline minimum of 326.3 Wh mol^{-1} (**Fig. S5**). When the pH was increased to 2 and 3, although the Cr(VI) removal efficiency remained near 100%, the initial reduction ratios (0–10 min) dropped to approximately 80% and below 60%, respectively. This temporal divergence (time-lag) between apparent removal and intrinsic reduction indicated that the decrease in proton concentration significantly increased the interfacial charge transfer resistance for the electron transfer. After an initial kinetic adaptation period, the EE recovered to above 80% and 75%, respectively, and the SEC stabilized at around 500 Wh mol^{-1}. As the solution pH further increased to 4, the low-potential CrO_4^{2-} became the dominant species, and the lack of interfacial protons fundamentally blocked the PCET pathway. The 50% removal efficiency observed in the initial stage at pH = 4 likely originated from physical adsorption by the porous carbon; following adsorption saturation, the removal efficiency experienced a breakthrough, plummeting to roughly 15%. From a reaction engineering perspective, the proton deficiency caused a sharp decline in the apparent charge transfer rate, shifting the system from a mass-transfer-controlled regime to a kinetic-controlled regime. Concurrently, the hindered Cr(VI) reduction meant that the excess cathodic current driven by the constant voltage was consumed by side reactions such as HER. This caused the EE of the pH = 4 system to drop below 10%, while the SEC increased to ~6000 Wh mol^{-1}.

The adjustment of the volumetric flow rate effectively reflects variations in the reactor's treatment throughput (Fig. 2g and **Fig. S6**). In a flow-through porous reaction process, perturbing the flow rate (Q) essentially modulates two core transport parameters: the apparent volumetric mass transfer coefficient ($k_m \cdot a_e$) and the τ (**Table S4**). To accurately analyze the impact of hydrodynamics on electro-reduction, the ε of the monolithic carbon electrode was measured to be 84.97%. This porosity, combined with the aforementioned through-hole structure, minimized fluid permeation resistance. Based on this void volume, the dimensionless mass-transfer Da number was introduced to investigate the relationship between mass transfer and reaction kinetics. At a low flow rate (3 mL min^{-1}), the system possessed a prolonged τ (17.44 s). The resulting high characteristic Da (≫ 3.0) provided a redundant reaction window for the pollutants, maintaining the removal at >99%. However, energy calculations revealed that the EE was below 20%, and the SEC escalated to 2000–4500 Wh mol^{-1} (**Fig. S6**). The coexistence of high conversion and low efficiency occurred because the excessively low influent flow rate placed the interface in a considerable concentration polarization regime. Driven by a constant voltage, a large fraction of cathodic electrons unconsumed by the substrate was dissipated in side reactions such as HER. By moderately increasing the flow rate to an intermediate range (6–12 mL min^{-1}), the flow-through forced convection effectively compressed the diffusion boundary layer at the solid-liquid interface, significantly enhancing $k_m \cdot a_e$ (0.608–0.897 s^{-1}) and compensating for the shortened τ (8.72–4.36 s). Under these conditions, the system maintained an appropriate dimensionless kinetic boundary ($Da = 3.91$), ensuring the synergy between the apparent mass transfer rate and the electron transfer rate. Consequently, the removal efficiency remained at >99%, the EE rose to ~80%, and the SEC stabilized at a low level of 350–500 Wh mol^{-1}. However, when the flow rate increased to 15 mL min^{-1}, the Cr(VI) removal efficiency rapidly declined to ~82%. This decay behavior was analyzed through the evolution of Da. Because k_m in porous media grows with flow rate ($k_m \propto Q^b$, $b < 1$), whereas the actual residence time is proportional to flow rate ($\tau \propto Q^{-1}$), the characteristic Da decreased following a negative power-law relationship with increasing flow rates ($Da \propto Q^{b-1}$). Quantitative calculations indicated that under the short τ (3.49 s) at 15 mL min^{-1}, the system's Da dropped to approximately 1.71, which is far below the theoretical threshold required for >95% conversion. This analysis demonstrated that under the CV mode with limited polarization potential, a fast fluid flow caused the substrate to breakthrough before completing the PCET process, thereby leading to decreased activity and increased SEC.

In addition to the constraints of the hydrodynamic characteristic time, the influent concentration directly determines the absolute mass flux transported to the electrode interface. The impact of influent concentration (10–90 mg L^{-1}) was systematically investigated under the CV mode (Fig. 2h and **Fig. S7**) to further reveal the relationship between mass transfer and reaction kinetics. Under low to moderate concentration conditions (10–30 mg L^{-1}), the system similarly exhibited characteristics of high conversion and low EE. As shown in Fig. 2h, both the removal efficiency and intrinsic reduction ratio were stably maintained near 100%. From a reaction engineering perspective, if the charge transfer rate at low concentrations is significantly greater than the apparent mass transfer rate, the reaction strictly operates in a mass-transfer-controlled regime. The system's Da ≫ 3.0 ensured the complete removal of the pollutant. However, energy consumption data indicated that due to the minimal absolute mass flux of the substrate, the cathodic electron flux generated under constant voltage (4 V) was in substantial stoichiometric excess. This intensified the HER side reaction, causing the EE to hover around 20% and the SEC to reach 1400–1600 Wh mol^{-1}. As the influent concentration was elevated to 50–90 mg L^{-1}, the kinetic and energetic metrics reversed. At a high concentration of 90 mg L^{-1}, the EE approached 100%, and the SEC dropped substantially to the 200–300 Wh mol^{-1} range. According to Fick's first law, the high bulk concentration greatly enhanced the concentration gradient for intra-pore diffusion, effectively mitigating concentration polarization. The abundant interfacial substrate rapidly captured the available electrons, maximizing the efficiency. Nevertheless, the steady-state removal efficiency under the 90 mg L^{-1} condition dropped to approximately 40% (although the intrinsic reduction ratio

remained above 90%, proving that the ions diffusing to the catalyst surface were effectively converted) (Fig. 2h).

Beyond these steady-state macroscopic behaviors, the early-stage transient kinetics under extreme limits warrant specific attention. Under non-optimal conditions like pH 4 (Fig. 2f) or 90 mg L^{-1} (Fig. 2h), the value of R_{red} initially dropped before recovering. According to **Eq. 3**, rapid physical adsorption in the first 5 min causes a large total removal (a rapidly increasing denominator). At the same time, actual Faradaic reduction is initially slow due to a lack of protons or high substrate concentration (a small numerator), leading to the initial drop. As the continuous reaction proceeds, protons generated by the anodic OER are transported to the cathode, which speeds up the reduction and allows R_{red} to recover and stabilize. In contrast, the value of EE at 1 V showed an opposite trend. EE is calculated based on the total input charge (**Eq. 7**, Fig. 2d). At 1 V, a large portion of the early current is consumed by non-Faradaic double-layer charging rather than actual Cr(VI) reduction. Once the double layer is charged, the Faradaic reduction reaction briefly takes over, raising EE. However, since 1 V is too low to drive continuous fast reduction against mass-transfer resistance, EE eventually decreases to a lower stable value.

To further evaluate the practical applicability of the continuous-flow FES, the interference effects of coexisting ions found in effluents were systematically investigated. As depicted in **Fig. S8**, the continuous electro-reduction of Cr(VI) was conducted in the presence of various background anions (NO_3^-, CO_3^{2-}, Cl^-, PO_4^{3-}) and cations (K^+, Mg^{2+}, Ca^{2+}). Remarkably, the Cr(VI) removal efficiency remained highly stable, ranging from 96.9% to >99% across all simulated complex water matrices. This negligible impact provides compelling evidence that Cr(VI) detoxification in the present system is driven by targeted faradaic PCET rather than non-specific physical adsorption.

3.3. Activity in the CC mode with electron flux matching strategy

It should be noted that while calculating the applied current based on the stoichiometric requirement of the Cr(VI) mass flow is fundamentally rooted in conventional Faraday's Law, maintaining this theoretical flux in a continuous flow-through system with ultra-short residence times poses a kinetic challenge. The objective of this strategy is not theoretical derivation, but rather to evaluate whether the dynamically polarized solid-liquid interface can accommodate the forced electron flux to compensate for mass-transfer limitations, and to quantify the associated energetic trade-offs. Compared to the aforementioned CV mode, the CC mode enables direct and precise control over the electron flux at the liquid-solid interface. However, the CC mode is highly sensitive to the intrinsic reaction kinetics of the solid-liquid interface; if the forced electron flux exceeds the interfacial reaction limit, the excess electrons lead to a negative shift in the electrode polarization potential, resulting in the considerable side reactions [48,49]. In light of this, an electron flux matching strategy was introduced in this study. Specifically, the applied operating current was dynamically adjusted to precisely approximate the theoretical stoichiometric equivalent based on the absolute mass flow of Cr(VI) entering the FES reactor (which is governed by the influent concentration and flow rate). Under these parametric boundaries, the regulatory effects of the fluid microenvironment and treatment throughput on the reactor performance were investigated.

Under the current-matching strategy, the regulatory role of solution pH on interfacial electron transfer was first examined (**Fig. 3a** and **b**). When the system operated under strongly acidic conditions (pH 1–2), highly consistent reaction synergy was observed: the Cr(VI) removal efficiency and intrinsic reduction ratio coincided after a brief adaptation period and remained steady at ~100%. Concurrently, the EE hovered near the theoretical maximum of 100%, and the SEC stabilized at a low baseline of 150–200 Wh mol^{-1} (Fig. 3b). This confirmed that, given an abundant proton supply, the intrinsic interfacial reaction rate could fully accommodate and consume the galvanostatically supplied electron flux. However, as the pH increased, significant kinetic deviations occurred. During the initial stage (< 10 min) at pH 4, the system maintained a removal efficiency of near 100%, yet the concurrent reduction ratio was almost zero. This indicated that the initial pollutant removal relied entirely on capacitive/physical adsorption by the porous carbon

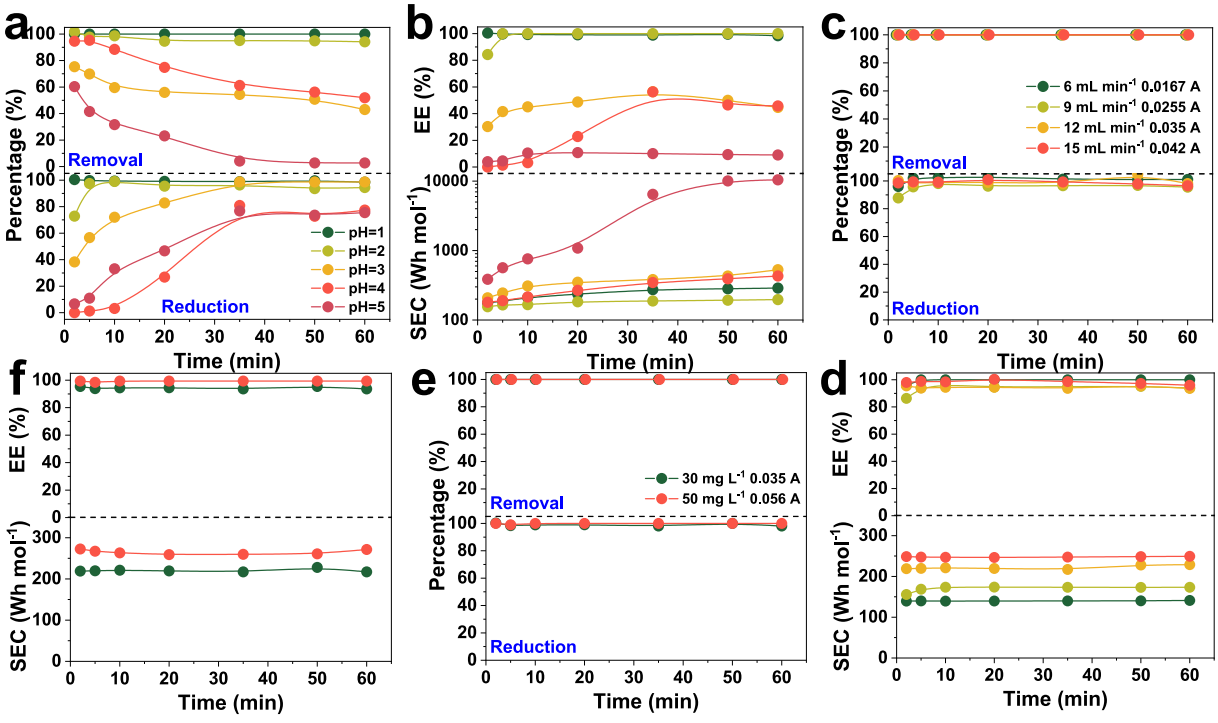

Fig. 3. Effects of (a, b) initial pH, (c, d) volumetric flow rate, and (e, f) initial concentration on the electro-reduction performance of Cr(VI) in the flow-through system under the CC mode. Panels (a, c, e) display the time-dependent removal percentages and reduction ratios, while panels (b, d, f) present the corresponding EE and SEC.

skeleton. As the polar sites became saturated, the steady-state removal efficiency decreased to approximately 50%, and the reduction reaction was sustained at only 80%, causing the EE to drop into the 50% range. At pH 5, both the steady-state removal and reduction ratios rapidly declined to below 10% and near zero, respectively, with the EE approaching zero. Notably, the SEC curve at pH 5 exhibited an exponential surge (Fig. 3b), eventually exceeding 10,000 Wh mol^{-1}. This phenomenon reveals the underlying mechanism of the CC mode: because the system must pass a predetermined faradaic current per unit time, the proton deficiency at high pH blocked the targeted electron transfer pathway, rendering the electrode unable to consume electrons via the primary reaction. According to polarization principles, the electrode potential was forced to shift substantially negatively to maintain the set current, resulting in the input electrical energy being almost entirely dissipated in parasitic reactions such as HER. This quantitative analysis corroborates that the current-matching strategy must be strictly confined within an appropriate thermodynamic pH window to prevent exorbitant energy consumption.

The impacts of different volumetric flow rates (Fig. 3**c** and **d**) and influent concentrations (Fig. 3**e** and **f**) on reactor performance and energy consumption were systematically evaluated. When the flow rate was increased from 6 to 15 mL min^{-1}, or the influent concentration was elevated from 30 to 50 mg L^{-1}, the operating currents were proportionally and dynamically upregulated (from 0.0167 A to 0.042 A for flow rates, and from 0.035 A to 0.056 A for concentrations). Consequently, both the removal and reduction ratios were stably maintained at >99% throughout the operational cycles. This apparent complete conversion sharply contrasts with the kinetic breakthrough readily observed under high loads in the aforementioned CV mode. From a reaction engineering perspective, this phenomenon elucidates the dynamic polarization compensation mechanism of the load-matched CC mode against the classic dimensionless *Da* number limitations. In the CV mode, a short fluid residence time (τ) causes the *Da* value to drop below the critical threshold, causing the breakthrough. Similarly, a surge in influent concentration leads to an electron-limited regime due to insufficient electron supply under constant polarization. However, in the CC mode, to deliver the forcibly applied high-throughput electron flux (e.g., 0.042 A at 15 mL min^{-1}), the system drove a high cathodic η_{act}. This interfacial driving force enhanced the apparent charge transfer rate, elevating the intrinsic reaction rate to match the surging mass flux. Thus, the apparent reaction rate imparted by the forced CC polarization compensated for the apparent mass-transfer limitations caused by the ultra-short residence time. It is crucial to note that the characteristic *Da* derived herein is strictly bounded by the assumption of a pure mass-transfer-controlled regime. As detailed in **Table S4**, because the strong galvanostatic polarization altered the interfacial kinetics, the system deviated from a mass-transfer-controlled state. Consequently, the classical *Da* formulation was no longer physically applicable for quantitative prediction under the CC mode (denoted as N/A in **Table S4**), serving instead as a comparative baseline to highlight the severity of the mass-transfer constraints. Nevertheless, the analysis of energy consumption data unveiled the energetic cost of this process. In the aforementioned high-load regions, the EE of the system (Fig. 3**d** and 3**f**) closely aligned with the >99% theoretical limit, demonstrating that the precisely matched electrons were targeted entirely for Cr(VI) reduction, with negligible diversion toward side reactions such as HER. Simultaneously, however, the SEC of the system exhibited a pronounced step-wise escalation with increasing flow rate or concentration: an increase in flow rate drove the SEC from 140 to 250 Wh mol^{-1}, while elevated concentration pushed the SEC from 220 to approximately 270 Wh mol^{-1}.

Unlike the CV mode, processing higher Cr(VI) concentrations in the CC mode increases the SEC. Since SEC is proportional to U/EE (**Eq. 8**), applying a larger matching current to handle a higher mass flux raises the value of U. This higher voltage is required to overcome both the increased Ohmic drop and the higher η_{act} needed for a faster reduction rate. Through this dynamic polarization, the CC mode effectively compensates for mass-transfer limitations under short residence times (low *Da* conditions), maintaining complete Cr(VI) removal at the cost of higher SEC. The fundamental limits of these two modes are further clarified by two-electrode I-V curves (**Fig. S9**). It should be noted that two-electrode measurements reflect the coupled polarization of both electrodes rather than isolated half-cell overpotentials. Under the CV mode, the applied cell voltage is fixed (e.g., 4 V). Because the overall driving force is bounded, a higher cell impedance (as observed for MCM-900) restricts the current (~0.23 A vs. ~0.37 A for o-MCM-900), indicating that the throughput under CV mode is largely constrained by the overall cell resistance. Conversely, the CC mode forcibly maintains a constant total current flux (I_{total}). For an electrode with a smaller electroactive surface area, the true local current density ($i_{local} = I_{total}/ECSA$) increases substantially. To maintain a target current of 0.13 A, MCM-900 requires a cell voltage approximately 0.6 V higher than that required by o-MCM-900 (~2.9 V vs. ~2.3 V). Given their nearly identical R_s, this extra 0.6 V predominantly reflects the elevated combined activation overpotential required to drive charge transfer across fewer active sites, suggesting that the CC mode is primarily governed by interfacial activation constraints.

To evaluate its practical potential, the o-MCM system was compared with reported electrochemical Cr(VI) reduction technologies (**Table S5**). Our system under the CC mode (12 mL min^{-1}) achieves complete Cr(VI) removal (> 99%) while maintaining a high EE (> 99%). While flow-by or 3D particle systems (Entry 2) improve mass transfer, their thick diffusion layers and side reactions often result in low electron efficiency (EE < 30%). Other flow-through systems (Entries 3–8) handle higher flow rates but still face a trade-off, typically limiting EE to 40–85% to maintain high removal. Traditional batch flat-plate reactors (Entries 9–11) suffer from slow diffusion, requiring long treatment times. This demonstrates that matching the forced current with mass transfer effectively suppresses side reactions, offering a highly efficient approach for continuous wastewater treatment.

3.4. Mechanistic exploration of materials carbonized at different temperatures

To elucidate the underlying driving mechanisms by which the intrinsic structure of the carbon substrate affects the flow-through electro-reduction efficiency of Cr(VI), this study systematically investigated the evolution of the physicochemical properties of monolithic mesoporous carbons (o-MCM-T) carbonized at varying temperatures (800–1100 °C). The results indicate that the carbonization temperature strictly governs the structural and chemical transformations during the conversion of the polymer precursor into the inorganic carbon skeleton.

Morphologically, all o-MCM-T samples retained the 3D continuous macroporous framework constructed by cross-linked carbon nanoparticles, ensuring the essential hydraulic permeability for a flow-through electrode (Fig. 4a-d). However, nitrogen adsorption-desorption isotherms revealed a distinct “volcano-like” trend in the specific surface area with increasing pyrolysis temperature. When the temperature was raised from 800 to 900–1000 °C, the exhaustive release of volatile components from the precursor established a highly developed mesoporous network. Consequently, the specific surface area increased from 667.45 $m^2\ g^{-1}$ to 744.46 $m^2\ g^{-1}$, with the 1000 °C sample achieving the maximum surface area and pore volume (**Table S6**). Nevertheless, as the carbonization temperature was further elevated to 1100 °C, the isotherm shifted significantly downward, indicating that the carbon skeleton underwent profound graphitic shrinkage at extreme temperatures. This led to the collapse of internal mesopores, resulting in a substantial plunge in the specific surface area to 346.75 $m^2\ g^{-1}$. Raman spectroscopy demonstrated that the value of the I_D/I_G exhibited a marginal upward trend from 0.89 to 0.99 as the temperature increased (Fig. 4f). For polymer-derived amorphous carbons, this evolution signifies the nucleation and growth of

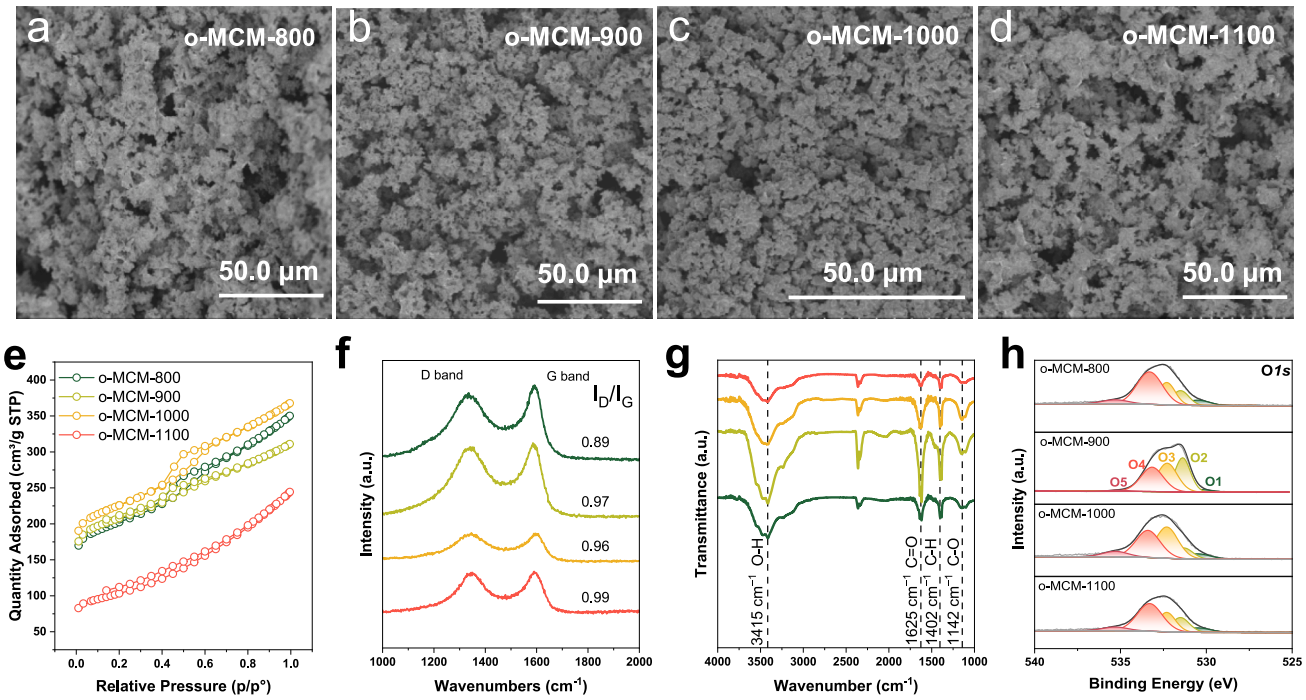

Fig. 4. SEM images of o-MCM materials carbonized at (a) 800 °C, (b) 900 °C, (c) 1000 °C, and (d) 1100 °C. (e) Nitrogen adsorption-desorption isotherms, (f) Raman spectra, (g) FTIR spectra, and (h) high-resolution O 1 s XPS spectra of the carbon materials prepared at different carbonization temperatures.

nanocrystalline graphite domains within the amorphous matrix, which inherently enhances the bulk electrical conductivity of the material.

Beyond physical restructuring, the surface chemical reactivity was also strongly temperature-dependent. FTIR spectra revealed that as the temperature increased from 800 to 1100 °C, the intensities of the characteristic absorption bands corresponding to polar oxygen-containing groups (e.g., O—H, C═O, and C—O) initially intensified and subsequently diminished (Fig. 4g). This trend was quantitatively corroborated by XPS analysis (**Fig. S10** and **Table S6**). The surface oxygen concentration of the carbon materials escalated from 6.09 at.% to a peak of 16.59 at.% (for o-MCM-900), and then gradually declined to 5.33 at.%. High-resolution O 1 s XPS spectra further confirmed that the oxygen speciation on the o-MCM surfaces underwent distinct alterations across the evaluated carbonization temperatures (Fig. 4h). When the temperature exceeded 900 °C, thermal deoxygenation led to the gradual desorption of polar oxygen-containing groups (**Table S7**). Specifically, the relative proportion of thermally labile carboxyl groups (O2), which act as crucial proton donors, decreased sharply from a peak of 34.61% in o-MCM-900 to 17.73% in o-MCM-1100. This extensive loss of polar functional groups not only reduced the hydrophilicity of the carbon skeleton but also depleted the critical receptors and active sites required for Cr(VI) adsorption and subsequent electron transfer [50–52].

Based on the microstructural analysis of the carbon skeletons, the synthesized o-MCM-T materials were integrated into the continuous-flow FES to evaluate their performance and energetic evolution under both CV and CC modes. In the CV mode (**Fig. 5a** and **b**), an adequate hydraulic residence time (4.03 s, corresponding to 12 mL min^{-1}) largely masked the kinetic differences among the materials. The electrodes prepared across all carbonization temperatures (800–1100 °C) exhibited high Cr(VI) electro-reduction capabilities, with steady-state removal efficiencies approaching 100% and reduction ratios exceeding 80%. This observation indicated that all the fabricated monolithic porous carbons possessed the fundamental physical properties required for Cr(VI) detoxification. However, the system's energy consumption data unveiled significant energetic disparities among the materials (Fig. 5b). The EE and SEC exhibited pronounced bifurcations: o-MCM-900 demonstrated the optimal comprehensive performance, achieving a steady-state EE of approximately 80% and maintaining the SEC at an exceptionally low baseline of 350–400 Wh mol^{-1}. In contrast, carbonization temperatures that were either too low (800 °C) or too high (1000 °C and 1100 °C) caused the EE to drop to roughly 60% and the SEC to increase to the 500–600 Wh mol^{-1} range.

These energetic divergences were mechanistically elucidated through basic electrochemical characterizations. Cyclic voltammetry scans revealed that the 900 °C sample possessed the highest specific capacitance (0.58 F g^{-1}) (**Table S8**). This suggested the formation of a highly developed mesoporous network retaining moderate polar functional groups during pyrolysis, thereby maximizing the ECSA and interfacial wettability. Furthermore, EIS confirmed that this sample exhibited the smallest semicircle diameter, corresponding to the lowest R_{ct}. It also displayed a steeper Warburg impedance tail in the low-frequency region, corroborating favorable interfacial electron transfer rates and intra-pore ion diffusion capabilities. By comparison, although the 800 °C sample retained relatively high capacitance, its insufficient graphitization hindered free electron transport within the carbon lattice, resulting in the highest charge transfer resistance (4.76 Ω). Conversely, when the carbonization temperature was elevated to 1000 °C and 1100 °C, despite the enhanced graphitization, the contracted cyclic voltammetry integrated area indicated the collapse of internal mesopores and the loss of surface polar oxygen-containing sites. These variations of the structure and surface functionalities directly elevated their R_{ct} values to 3.36 Ω and 3.28 Ω, respectively. Therefore, under the CV mode with a fixed applied voltage, the increased bulk and interfacial resistances led to a larger portion of the electrical energy being dissipated to overcome internal Ohmic drops rather than driving the target faradaic reduction. This insufficient effective polarization facilitated parasitic side reactions (such as water electrolysis), which diminished the faradaic selectivity and consequently drove up the overall SEC.

In the load-matched CC mode, all samples achieved a removal efficiency approaching 100%, and the EE for all systems closely aligned with the 100% theoretical limit (Fig. 5c). This demonstrated that under the rigid current constraint of the CC mode, all carbon skeletons could effectively minimize gas-evolving side reactions and achieve high faradaic selectivity, provided that adequate fluidic conditions were

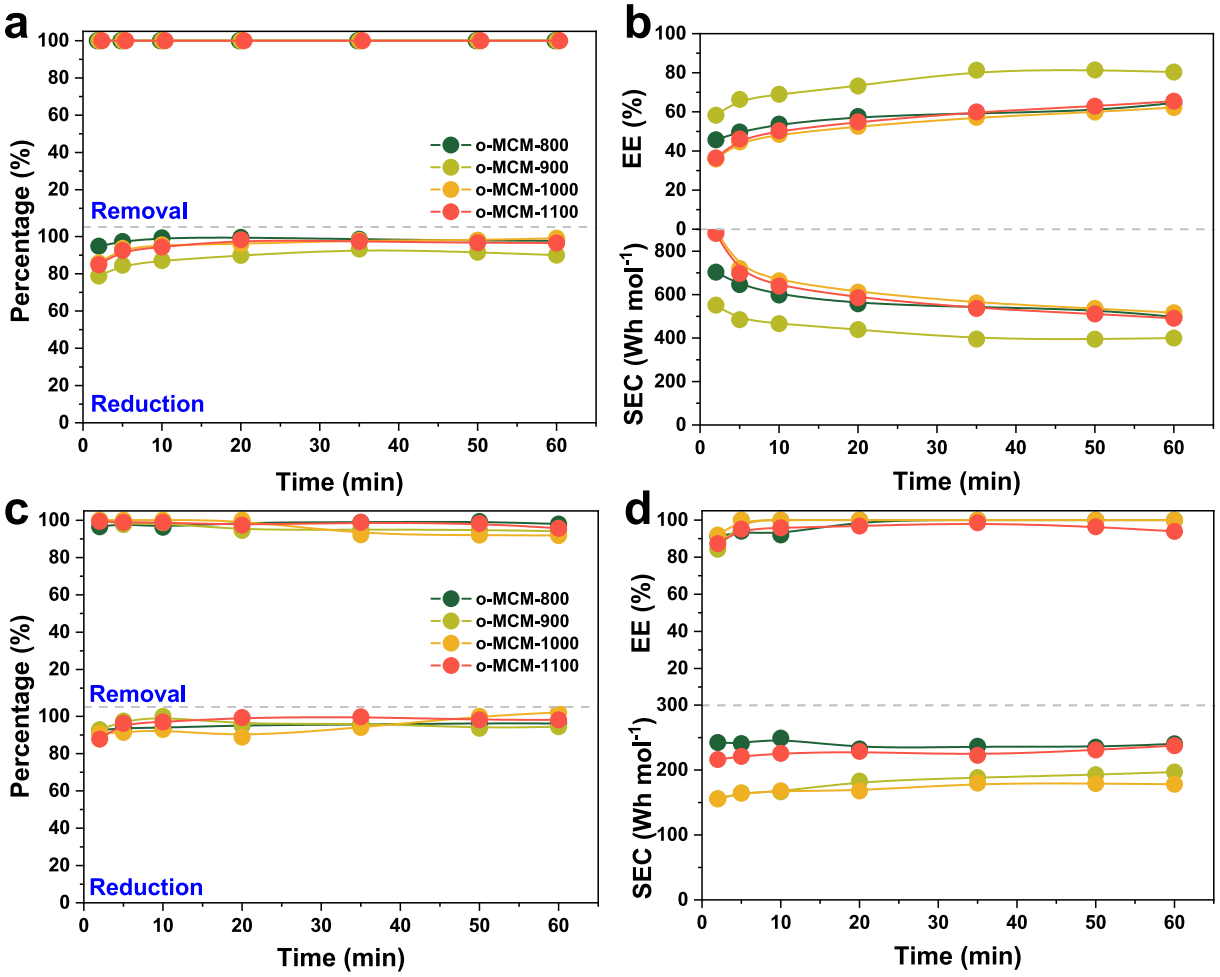

Fig. 5. Electro-reduction performance of Cr(VI) using electrode materials carbonized at different temperatures under (a, b) CV and (c, d) CC modes. Panels (a, c) display the removal and intrinsic reduction percentages, while panels (b, d) illustrate the corresponding EE and SEC.

maintained. However, despite the highly consistent conversion and selectivity, the SEC still exhibited significant variance (Fig. 5d). Given the strict proportionality SEC∝U/EE, when the EE approaches 100%, the vertical differentiation in SEC is entirely governed by the differences in the applied voltage required to sustain the predetermined constant current. Quantitative results indicated that the most active sample, o-MCM-900, consistently maintained the lowest SEC baseline of approximately 150–190 Wh mol^{-1}. Materials deviating from this optimal carbonization temperature suffered energetic penalties. Specifically, the 800 °C sample (240–280 Wh mol^{-1}) elevated the applied voltage to overcome its intrinsic R_{ct} (4.76 Ω). Similarly, the over-graphitized 1100 °C sample (210–230 Wh mol^{-1}) was forced to drive up the interfacial η_{act} to compensate for its limited ECSA and the scarcity of proton-donor sites.

3.5. Cross-swap experiments

To thoroughly elucidate the structure-performance relationship of the carbon electrodes in the flow-through reactor and to define the global rate-determining step within the two-electrode series system, asymmetric anode-cathode cross-swap experiments were designed. A highly conductive but surface-inactive carbon material (MCM-900) and a highly active optimized material (o-MCM-900) were selected. By systematically tracking the activity, efficiency, and energy consumption of different electrode combinations under CV and CC modes, the synergistic mechanisms between fluid transport and anodic/cathodic half-reactions were analyzed. As a baseline, the symmetric system employing o-MCM-900 on both sides exhibited the optimal comprehensive performance (steady-state removal near 100%, with the lowest and most stable SEC). Conversely, the symmetric MCM-900 system yielded a removal efficiency of only ~10%, restricted by strong surface hydrophobicity and an absence of active sites, thereby validating the necessity of surface modification.

3.5.1. CV mode

Under the CV driving mode, the partitioning of the constant applied voltage between the anode and cathode directly dictates the activation extent of each half-reaction. As shown in Fig. 6a, the steady-state removal efficiency of the anode (o-MCM-900) / cathode (MCM-900) combination was maintained at approximately 60%. For the reverse configuration (anode (MCM-900) / cathode (o-MCM-900)), despite possessing a theoretically superior cathodic reduction interface, its apparent removal efficiency remained near 100%, but this was decoupled from its faradaic conversion. EE analysis (Fig. 6b) revealed that the EE of the anode (MCM-900) / cathode (o-MCM-900) combination dropped to ~20%, with the SEC increasing to 1500–2000 Wh mol^{-1}. In contrast, the EE of the anode (o-MCM-900) / cathode (MCM-900) combination was maintained at ~35%, and its SEC significantly decreased to below 1000 Wh mol^{-1}. These results indicate that in the flow-through reactor, the anodic oxidation reaction predominantly governs the overall activity. In the reduction pathway, the conversion of Cr(VI) at the cathode is highly dependent on proton supply. In this system, apart from the trace HCl added, the sole in-situ proton source is the anodic oxygen evolution reaction (OER, $2H_2O \rightarrow O_2 + 4H^+ + 4e^-$)

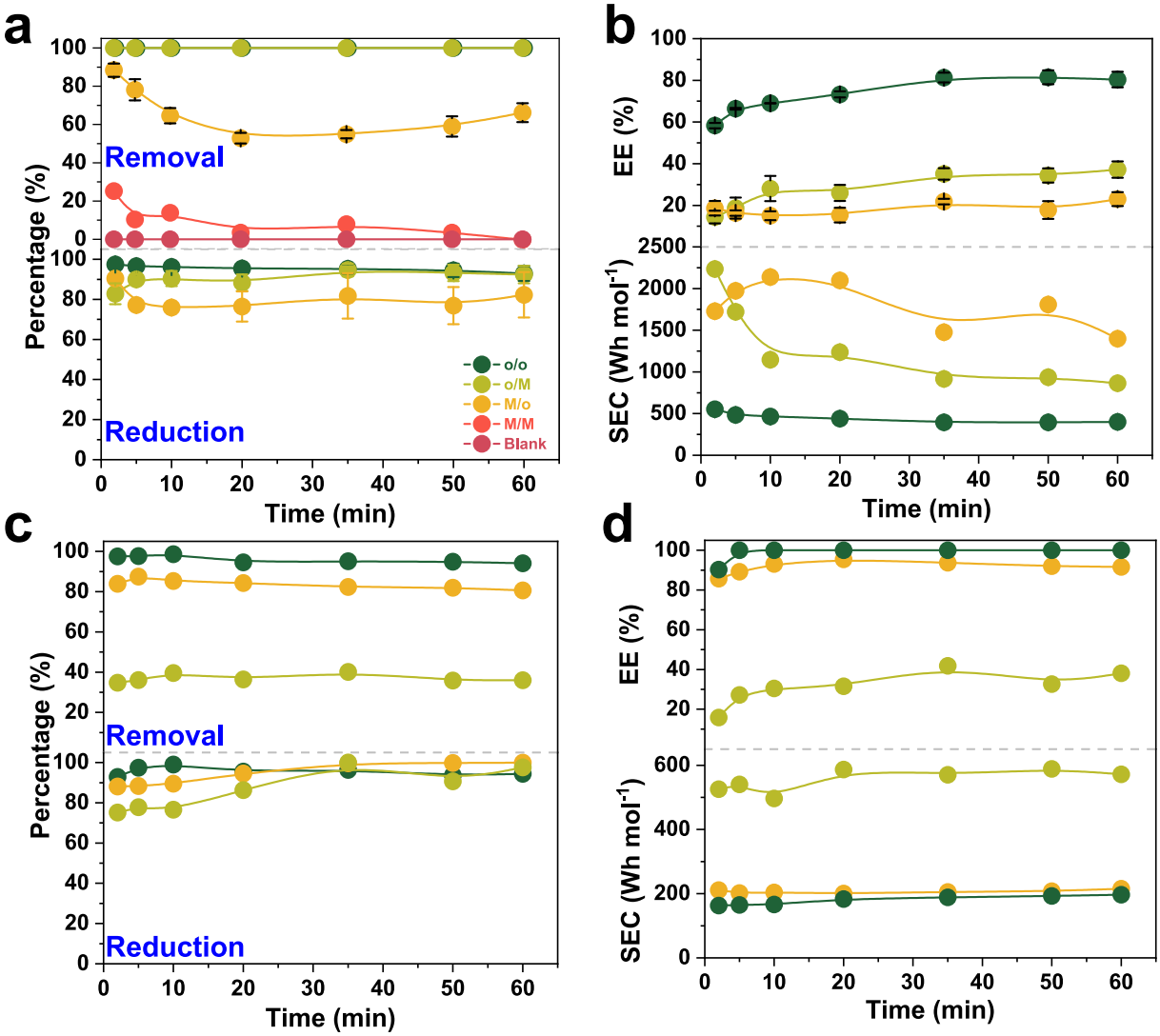

Fig. 6. Performance comparison of the flow-through reactor with cross-swapped anode and cathode materials under different driving modes. Time-dependent (a) removal efficiency and reduction ratio, and (b) corresponding EE and SEC under the CV mode. Time-dependent (c) removal efficiency and intrinsic reduction ratio, and (d) corresponding EE and SEC under the CC mode. *("o" represents the optimized o-MCM900, while "M" represents the unmodified MCM900. The configuration format "X/Y" denotes the anode/cathode arrangement).*

[53]. When the system employed the unoxidized MCM-900 as the anode, it exhibited a high OER overpotential and large polarization resistance, which restricted the overall circuit current under a fixed voltage (4 V). In addition, because Cr(VI) reduction relies on a proton-coupled electron transfer (PCET) process (as demonstrated by the pH-dependent tests in Fig. 2f), the sluggish OER kinetics on MCM-900 may also limit local proton generation. Therefore, the poor performance of this combination was likely a combined outcome of high cell resistance, restricted electron flux, and potentially insufficient proton supply to the downstream cathode. Under these electron- and proton-limited conditions, the observed apparent removal (> 99%, yellow curve in Fig. 6a) was mainly driven by transient physical/capacitive adsorption rather than continuous Faradaic reduction, resulting in a low EE (~20%) and high SEC (1500–2000 Wh mol^{-1}). Conversely, when the more active o-MCM-900 was used as the anode, its lower polarization resistance facilitated overall current flow and sustained more efficient OER activity. This not only provided a higher driving potential for the downstream MCM-900 cathode but also supported the requisite proton environment, improving the removal efficiency to ~60%, elevating the EE to 37.18%, and lowering the SEC to 865 Wh mol^{-1}.

3.5.2. CC mode

Under the CC driving mode, the system forces the input of a predetermined theoretical electron flux. Thus, the rate-determining step shifted fundamentally from the overpotential limitation in the CV mode to the interfacial electron capture rate. As depicted in Fig. 6**c** and **d**, quantitative experiments revealed two distinct mechanisms by which the anode and cathode interfaces responded to forced polarization.

Firstly, the cathodic active sites determine the faradaic selectivity of the system, while the anodic overpotential dictates voltage loss. The anode MCM-900 / cathode o-MCM-900 combination maintained a steady-state reduction ratio in the range of 80%–85% with an EE as high as ~90%. This performance sharply contrasts with its inefficiency under the CV mode. Mechanistically, to sustain the forced current in the CC mode, the system passively elevated the applied voltage, thereby intensifying the OER rate on the MCM-900 anode surface to provide sufficient protons. Simultaneously, the abundant polar groups on the o-MCM-900 cathode effectively consumed the forced electron and proton fluxes. Although this system achieved efficient conversion, the additional voltage required to overcome the MCM-900 anode barrier led to an increase in energy consumption (SEC slightly higher than that of the symmetric optimal group). Secondly, employing MCM-900 as the

cathode initiated the gas-evolving side reactions and in-situ activation effects. The anode o-MCM-900 / cathode MCM-900 combination exhibited a restricted removal capacity (35%–40%), and its SEC increased to over 500 Wh mol^{-1}. An in-depth analysis of this energetic decline reveals that, although the o-MCM-900 anode effectively promoted proton generation, the strong hydrophobicity of the unoxidized MCM-900 cathode prevented the interfacial Cr(VI) from timely capturing the forced electron flux. To maintain the constant current, the cathode was forced to initiate the HER. The substantial amount of electrical energy was diverted to generate hydrogen gas, resulting in a low initial EE (~38%) and a high SEC (~572 Wh mol^{-1}). However, the dynamic curves unveiled a notable in-situ activation phenomenon. As the HER and continuous polarization persisted, the intrinsic reduction ratio of this combination climbed from 75% to 95%, and the EE rose to approximately 40%. Although the limited physical porosity restricted the absolute treatment throughput, the PCET selectivity for the captured species was improved over time.

3.5.3. Discussions on the operations

By integrating the cross-swap experiments with microscopic electrochemical characterizations, this study establishes the rate-determining mechanisms of the porous flow-through reactor under different driving frameworks: CV mode is governed by surface Ohmic polarization, whereas CC mode is controlled by the interfacial activation. Moreover, o-MCM-900 displayed the optimal comprehensive performance across both modes, serving as an ideal mechanistic benchmark for assessing intrinsic structural adaptability under varying polarization fields.

Under the CV mode, the applied potential is fixed, and the faradaic current flux is restricted by the total impedance of the material. Aided by an appropriate graphitic skeleton, o-MCM-900 exhibited an low charge transfer resistance (3.3 Ω) in the EIS test. This low bulk and interfacial transport resistance enabled the applied voltage to effectively overcome the Ohmic drop (IR_{cell} drop), distributing a larger proportion of the voltage to the solid-liquid interface as effective η_{act} for driving electron transfer. Therefore, o-MCM-900 operated efficiently with minimal polarization dissipation. As a negative reference, the 800 °C sample, lacking sufficient graphitization, presented an R_{ct} of 4.76 Ω. This excessive impedance consumed the limited applied voltage via the bulk Ohmic drop, directly compressing the interfacial η_{act}. Meanwhile, its EE was as low as ~60%, and the SEC was pushed to 500–600 Wh mol^{-1}. This comparison clearly indicates that the apparent kinetic bottleneck in CV mode is the electron supply, and its efficiency highly depends on optimizing the carbon structure to minimize Ohmic polarization resistance.

Conversely, under the CC flux-matching mode, the current becomes a prerequisite, fundamentally shifting the rate-determining step to the charge capture and conversion capacity at the solid-liquid interface. Here, the local true current density (i_{Local}) becomes the core parameter governing energy consumption. o-MCM-900 exhibited the largest specific capacitance in the non-Faradaic region and a highly developed fluid-accessible wetted surface. This extensive physical contact area, combined with the high-density polar oxygen sites confirmed by XPS, maximized the distribution of the forced electron flux, avoiding a localized surge in i_{Local}. Consequently, this system smoothly delivered the target reduction current requiring only a minimal η_{act}, successfully controlling the SEC at approximately 150–190 Wh mol^{-1}. This interface-limited mechanism was validated by the over-graphitized 1100 °C sample. Despite its excellent electrical conductivity, the thermal loss of polar sites led to a significant decline in intra-pore wettability, drastically reducing the CV integrated area. Under the CC mode, this restricted contact area caused a remarkable increase in i_{Local}. To accommodate the quantitatively injected charge flux, the o-MCM-1100 material had to overcome interfacial resistance (R_{ct} = 3.28 Ω) by forcing a deep negative shift in local potential to provide an exceptionally high η_{act}, passively driving its SEC up to 210–230 Wh mol^{-1}.

Herein, quantitative analysis dictates that the design of practical electrochemical devices must be directionally optimized according to the external driving mode: potentiostatic systems must prioritize enhanced electrical conductivity to reduce Ohmic polarization, whereas galvanostatic systems must focus on improving surface wettability and chemical states to break through the limitations of interfacial activation.

3.6. Stability evaluation under continuous operation

In the engineering evaluation of continuous-flow electrochemical systems, the long-term viability of activity and the stability of system energy consumption are core prerequisites for scale-up applications. In this study, the FES was continuously operated for 400 min under both CC and CV modes (Fig. 7a). Over the 400 min operational period, the reaction activities of both driving modes were consistent: the Cr(VI) removal efficiencies were maintained near 100%, and the faradaic reduction ratios stabilized at approximately 90%, with no observable performance degradation or kinetic breakthrough. However, the long-term energy consumption data revealed differences in sustaining this conversion rate (**Fig. S11** and **S12**). Under the CC mode, the EE of the system remained close to the 100% theoretical limit, and the SEC stabilized within the range of 100–120 Wh mol^{-1}. In contrast, the energetic metrics of the CV mode decayed over the operational time: its EE gradually decreased from an initial ~80% to 64%, with a corresponding SEC increase from ~200 Wh mol^{-1} to 250 Wh mol^{-1}. This variation indicated that, compared to the CV mode where microenvironmental fluctuations induced side reactions, the strict control of charge flux in the CC mode effectively stabilized the long-term operation of the system. Furthermore, a 10-cycle alternating open-circuit and 4 V test explicitly decoupled physical adsorption from actual reduction (**Fig. S13**). Under open-circuit conditions, physical adsorption rapidly saturated within minutes. However, applying a 4 V potential instantly restored and maintained complete Cr(VI) removal. This dynamic test confirms that the sustained long-term removal is driven by Faradaic electro-reduction rather than physical adsorption.

Systematic characterizations for the used carbon materials were conducted. SEM images showed that after prolonged reaction and fluid shear, the three-dimensional macroporous network cross-linked by carbon particles maintained its structural integrity (Fig. 7b). Raman spectroscopy revealed a minor change in the I_D/I_G ratio (from 0.89 to 1.00), further confirming the structural stability of the bulk sp^2 conductive carbon matrix (Fig. 7c). The BET specific surface area of the used anode and cathode material decreased from 682.99 to 398.15 and 417.99 m^2 g^{-1}, respectively (Fig. 7e), suggesting that some micro/mesopores were likely filled or temporarily blocked by reaction intermediates. Considering the stable removal efficiency of the reactor, it could be inferred that despite the decrease in surface area, the macroporous channels responsible for fluid permeation remained unobstructed, and the residual pore network provided sufficient mass transfer and reaction sites.

In addition to the physical structure, the oxygen-containing functional groups at the anode and cathode interfaces exhibited distinct evolutionary patterns under the polarization electric field. FTIR spectroscopy visually reflected these changes (Fig. 7d). The pristine o-MCM-900 material displayed prominent absorption peaks around 3415 cm^{-1}, 1625 cm^{-1}, and 1142 cm^{-1}, corresponding to O—H stretching, C═O stretching, and C—O characteristic absorptions, respectively. After 400 min of operation, the absorption peak intensities corresponding to O—H and C—O in the anode sample weakened considerably, indicating a loss of oxygen-containing groups. Conversely, the infrared absorption features of the cathode sample were generally consistent with those of the pristine material. Specifically, the C═O and C—O peaks were well preserved, suggesting that the cathode interface possessed good chemical stability under the reducing electric field. Characterizations showed that the surface total oxygen content of the used anode carbon material decreased notably (from 16.59 at.% to 11.25 at.%), while the carbon

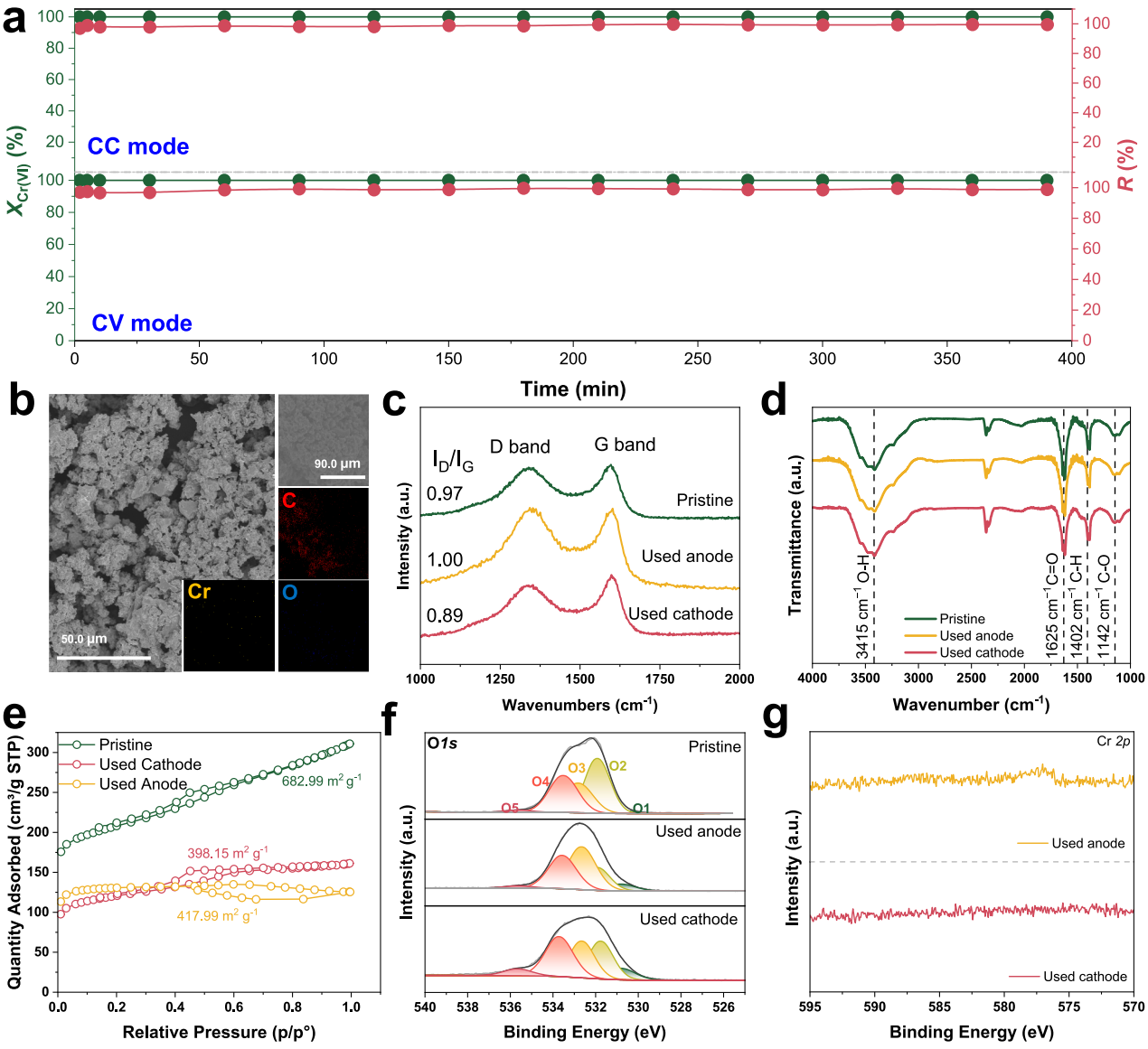

Fig. 7. (a) Performance of the flow-through electro-reduction of Cr(VI) under CC and CV modes over long-term operation. Characterizations of the materials after operation under the CC mode: (b) SEM image (inset: corresponding EDS elemental mapping), (c) Raman spectra, (d) FTIR spectra, (e) nitrogen adsorption-desorption isotherms, (f) deconvoluted high-resolution O 1 s XPS spectra, and (g) high-resolution Cr 2p XPS spectra.

atomic percentage relatively increased (from 83.20 at.% to 87.98 at.%) (**Fig. S14** and **Table S9**). From an electrochemical perspective, the anode was subjected to a high positive potential polarization for an extended period to drive the oxygen evolution reaction (OER). In such a highly oxidative microenvironment, some unstable polar oxygen-containing groups on the o-MCM-900 carbon skeleton readily underwent electrochemical decarboxylation or deep anodic corrosion, being oxidized into CO_2 or CO gases that escaped the interface [54]. Moreover, the synergistic effect of vigorous gas bubble evolution and hydrodynamic scouring during the OER further stripped away highly oxidized amorphous carbon fragments from the surface. Despite this anodic surface degradation, the system exhibits high fault-tolerance. Because the target Cr(VI) reduction occurs strictly at the cathode, whose polar groups are protected under the reducing field, the macroscopic performance remains stable as long as the bulk conductive network of the anode is intact. To verify this, an extended continuous test was conducted for 24 h. As shown in **Fig. S15**, the Cr(VI) removal efficiency remained highly stable at ~100%, confirming that the gradual anodic surface decarboxylation does not immediately compromise overall performance. Deconvolution of high-resolution O 1 s XPS spectra provided quantitative evidence for this process (**Table S10**). In the oxidative OER environment, the relative proportion of the O2 peak (carboxyl groups, -COOH) on the anode dropped from 34.61% to 19.03%, reflecting a electrochemical decarboxylation process that directly led to the decrease in total oxygen content. In electrochemical reduction reactions, the deposition and passivation of Cr(III) hydroxide gels at the electrode interface is a common cause of performance degradation. However, Cr 2p XPS spectra results demonstrated no apparent accumulation of Cr elements on the surface of the used carbon skeleton (Fig. 7b, g, and **S14**, **Table S9**). Calculating EE indirectly relies on the assumption that the generated Cr(III) does not accumulate on the electrode via physical adsorption or precipitation. Meanwhile, semi-quantitative EDS analysis was performed after the continuous operation as well. The residual Cr on both the used cathode (0.11 at.%) and anode (0.64 at.%) was observed. This confirms that Cr does not accumulate in the porous matrix, which is consistent with the high solubility of aqueous Cr^{3+} at pH 2. Because Cr is not trapped on the electrodes, the difference between influent total chromium and effluent Cr(VI) reflects the generated Cr(III). These results indicate that the applied current is predominantly consumed by Cr(VI) reduction under flux-matched

conditions with a high apparent Faradaic utilization. Moreover, although gas-phase products were not directly quantified, minor competing reactions such as HER might exist during the process. In summary, the physical stability of the conductive skeleton, the mass transfer rate driven by hydraulic shear, and the persistent interfacial chemical activity collectively maintained the stability of this system during long-term operation.

4. Conclusions

In summary, a continuous-flow FES centered on the o-MCM-900 materials was constructed, systematically elucidating the synergistic mechanisms among mass-transfer dynamics, interfacial reactions, and external driving modes during the electro-reduction of Cr(VI). The results substantiate that the highly efficient operation of porous electrodes relies on a delicate balance between the bulk conductive network and surface polar sites. The o-MCM-900 achieved a minimized charge transfer resistance (3.3 Ω), displaying a high activity of about >99% Cr (VI) removal efficiency and > 99% EE. Through the mechanistic decoupling via anode-cathode cross-swap experiments, the dominant polarization constraints for different operational modes were systematically elucidated: the CV mode is mainly governed by global cell resistance, whereas the CC mode is predominantly controlled by interfacial activation overpotentials. Herein, a dynamic electron flux matching CC operational strategy based on treatment throughput was proposed and validated. Aided by forced convection, this strategy successfully compensated for the mass-transfer limitations (which constrained the system to a theoretical $Da < 3$) under high hydraulic flow rates via dynamic polarization compensation. Remarkably, it maintained a near >99% removal rate and high EE even under low hydraulic residence times (high-flow-rate conditions). Concurrently, the engineering trade-off penalty for crossing this physical mass-transfer boundary was quantitatively revealed, demonstrating that dual polarization resistances drove up the applied voltage, leading to a passive escalation in SEC (e.g., from 140 to 250 Wh mol^{-1} at high flow rates). Furthermore, the high hydrodynamic shear forces generated within the flow-through channels effectively stripped away the reduction products, facilitating the in-situ self-cleaning of the electrode interface. This mechanism ensured zero breakthrough with a minimized SEC along with a high EE (> 99%) during a long continuous operation.

Declaration of competing interest

The authors declare that they have no known competing financial interests or personal relationships that could have appeared to influence the work reported in this paper.

Acknowledgements

We would like to acknowledge the financial support from the National Natural Science Foundation of China (22272056) and Guangdong Basic and Applied Basic Research Foundation (2026A1515010721). Research Fund Program of Guangdong Provincial Key Laboratory of Fuel Cell Technology (FC202305), and the start-up fund from Zhongkai University of Agriculture and Engineering.

Appendix A. Supplementary data

Supplementary data to this article can be found online at https://doi.org/10.1016/j.seppur.2026.140716.

Data availability

Data will be made available on request.

References

[1] W.S. Lei, M.L. Sun, W.L. Zhang, L.A. Liang, Z.Z. Ding, X. Tang, H.N. Dai, X.M. Liu, P.F. Qi, Y. Wang, Synergistic interfacial engineering of CNF@MN@MX composite membranes for highly efficient and recyclable photocatalytic detoxification of Cr (VI), Chem. Eng. J. 530 (2026) 173410, https://doi.org/10.1016/j.cej.2026.173410.
[2] E.A. Pasquali, C.E.D. Oro, J.L. Bernardi, L.D. Venquiaruto, H. Treichel, A.J. Mossi, R.M. Dallago, Adsorption of Cr(VI) by wet blue leather: sustainable solution for leather industry effluents, J. Water Process Eng. 69 (2025) 106807, https://doi.org/10.1016/j.jwpe.2024.106807.
[3] P. Adhya, S.S. Chowdhury, S. De, T. Mondal, M. Kaushal, Polymer-grafted silica based hybrid macrobeads for Pb(II) and Cr(VI) removal from water, Sep. Purif. Technol. 358 (2025) 130279, https://doi.org/10.1016/j.seppur.2024.130279.
[4] S. Pu, Y. Hou, C. Yan, H. Ma, H. Huang, Q. Shi, S. Mandal, Z. Diao, W. Chu, In situ Coprecipitation formed highly water-dispersible magnetic chitosan Nanopowder for removal of heavy metals and its adsorption mechanism, ACS Sustain. Chem. Eng. 6 (2018) 16754–16765, https://doi.org/10.1021/acssuschemeng.8b04028.
[5] S. Pu, Y. Hou, H. Chen, D. Deng, Z. Yang, S. Xue, R. Zhu, Z. Diao, W. Chu, An efficient photocatalyst for fast reduction of Cr(VI) by ultra-trace silver enhanced titania in aqueous solution, Catalysts 8 (2018) 251, https://doi.org/10.3390/catal8060251.
[6] W. Chen, Y. Tian, D. Liu, Y. Yi, X. Li, J. Wang, L. Bin, P. Li, B. Tang, L. Li, Unveiling the mechanism of enhanced water purification by F-Fe-Zn-MCM-41 in O_3/PMS, Appl. Catal. B Environ. Energy 345 (2024) 123608, https://doi.org/10.1016/j.apcatb.2023.123608.
[7] Y. Wang, T. Sun, L. Tong, Y. Gao, H. Zhang, Y. Zhang, Z. Wang, S. Zhu, Non-free Fe dominated PMS activation for enhancing electro-Fenton efficiency in neutral wastewater, J. Electroanal. Chem. 928 (2023) 117062, https://doi.org/10.1016/j.jelechem.2022.117062.
[8] M. Ye, G. Li, J. Liang, X. Liao, J. Ren, X. Fen, W. Qian, L. Li, S. Sun, A high-efficiency process for the separation of chromium and aluminum from waste aluminum sludge with a high chromium content using a combined oxidation and dispersion process, Sep. Purif. Technol. 258 (2021) 118083, https://doi.org/10.1016/j.seppur.2020.118083.
[9] J. Xiong, X. Yang, L. Xiao, S. Song, L. Cao, M. Xia, P. Wu, Y. Shi, K. Pi, G. Qiu, Enhanced electrochemical reduction and precipitation removal of Cr(VI) by a confined crystallization inducing cathode structure, Desalination 616 (2025) 119408, https://doi.org/10.1016/j.desal.2025.119408.
[10] C.M. Stern, T.O. Jegede, V.A. Hulse, N. Elgrishi, Electrochemical reduction of Cr (vi) in water: lessons learned from fundamental studies and applications, Chem. Soc. Rev. 50 (2021) 1642–1667, https://doi.org/10.1039/d0cs01165g.
[11] M.-L. Chen, X.-W. Yao, Z.-H. Diao, J.-C. Jin, W. Qian, Y.-Q. Yi, X. Chen, L.-J. Kong, Oxalic acid enhanced removal of heavy metal and pesticide by peroxymonosulphate activation with a green biochar iron composite: reactivity and mechanism, Sep. Purif. Technol. 327 (2023) 125013, https://doi.org/10.1016/j.seppur.2023.125013.
[12] H. Liu, G. Tian, W. Wang, J. Zhang, T. Wu, X. Ni, Y.-H. Wu, Carbon fiber-based flow-through electrode system (FES) for Cr(VI) removal at near neutral pHs via Cr (VI) reduction and in-situ adsorption of Cr (III) precipitates, Chem. Eng. J. 420 (2021) 127622, https://doi.org/10.1016/j.cej.2020.127622.
[13] X.-Y. Ni, Y.-H. Wu, H. Liu, X.-J. Zhang, Z.-B. Xu, L. Peng, W.-L. Wang, H.-B. Wang, Z. Chen, H.-Y. Hu, Enhancing disinfection performance of the carbon fiber-based flow-through electrode system (FES) by alternating pulse current (APC) with low-frequency square wave, Chem. Eng. J. 410 (2021) 128399, https://doi.org/10.1016/j.cej.2020.128399.
[14] F. Liu, Y. Liu, Q. Yao, Y. Wang, X. Fang, C. Shen, F. Li, M. Huang, Z. Wang, W. Sand, J. Xie, Supported atomically-precise gold nanoclusters for enhanced flow-through electro-Fenton, Environ. Sci. Technol. 54 (2020) 5913–5921, https://doi.org/10.1021/acs.est.0c00427.
[15] H. Liu, X.-Y. Ni, Z.-Y. Huo, L. Peng, G.-Q. Li, C. Wang, Y.-H. Wu, H.-Y. Hu, Carbon Fiber-based flow-through electrode system (FES) for water disinfection via direct oxidation mechanism with a sequential reduction-oxidation process, Environ. Sci. Technol. 53 (2019) 3238–3249, https://doi.org/10.1021/acs.est.8b07297.
[16] Y. Wang, J. Xu, H. Liu, Y. Lu, D. Chen, G. Lu, Square-wave alternating voltage for enhancing Cr(VI) reduction in a carbon Fiber-based flow-through electrode system, ACS EST Eng. 2 (2022) 831–841, https://doi.org/10.1021/acsestengg.1c00392.
[17] N. Olukayode, S. Ye, M. Hu, Y. Dai, Y. Yu, S. Sui, Exploring the asymmetrical configuration effects of anode and cathode flow field paths on proton exchange membrane fuel cell performance: a combined experimental and numerical modelling approach, J. Power Sources 666 (2026) 239131, https://doi.org/10.1016/j.jpowsour.2025.239131.
[18] Y. Sheng, W. Chen, M. Chen, F. Gong, B. Hou, C. Cheng, J. Mo, Z. Kang, Z. Xie, G. Yang, Unveiling proton pathways between the anode and cathode in PEM electrolyzer cells via direct reaction visualization, J. Mater. Chem. A 13 (2025) 27398–27404, https://doi.org/10.1039/d5ta03130c.
[19] M. Lohrengel, Potentiostat, in: G. Kreysa, K.-i. Ota, R.F. Savinell (Eds.), Encyclopedia of Applied Electrochemistry, Springer New York, New York, NY, 2014, pp. 1697–1702.
[20] A.A. Moya, A physically consistent electric circuit to interpret the galvanostatic charge-discharge curves of electric double layer capacitors, J. Power Sources 656 (2025) 238050, https://doi.org/10.1016/j.jpowsour.2025.238050.
[21] C. Costentin, J.-M. Savéant, Ohmic drop correction in electrochemical techniques. Multiple potential step chronoamperometry at the test bench, Energy Storage Mater. 24 (2020) 1–3, https://doi.org/10.1016/j.ensm.2019.07.029.

[22] L. Murphy, Galvanostatic cycling in battery research: a comprehensive guide to principles, Methods, and Applications, 2025.
[23] J. Ifthikar, Z. Chen, Z. Chen, A. Jawad, A self-gating proton-coupled electron transfer reduction of hexavalent chromium by core-shell SBA-Dithiocarbamate chitosan composite, J. Hazard. Mater. 384 (2020) 121257, https://doi.org/10.1016/j.jhazmat.2019.121257.
[24] M.H.V. Huynh, T.J. Meyer, Proton-coupled Electron transfer, Chem. Rev. 107 (2007) 5004–5064, https://doi.org/10.1021/cr0500030.
[25] B. Wang, Q. Jiang, G. Yang, H. Wang, H. Wang, F. Peng, H. Yu, J. Huang, G. Zhong, Y. Cao, Electric field-assisted uptake of hexavalent chromium ions with in situ regeneration of carbon monolith adsorbents, Adv. Sci. 10 (2023) 2301419, https://doi.org/10.1002/advs.202301419.
[26] J. Huang, B. Wang, H.-F. Wang, H. Wang, H. Yu, Y. Cao, Synergistic decontamination of hexavalent chromium and organic pollutants via dual-functional carbon monolith: deciphering Electrosorption-Electroreduction interplay, Sep. Purif. Technol. 382 (2026) 135773, https://doi.org/10.1016/j.seppur.2025.135773.
[27] M. Jiang, J. Huang, G. Yang, H. Wang, H.-F. Wang, F. Peng, Y. Cao, H. Yu, In-situ regeneration of carbon monoliths as an environmental-benign adsorbent for environmental remediation via a flow-through model, Sep. Purif. Technol. 314 (2023) 123542, https://doi.org/10.1016/j.seppur.2023.123542.
[28] G.-P. Hao, W.-C. Li, D. Qian, A.-H. Lu, Rapid synthesis of nitrogen-doped porous carbon monolith for CO_2 capture, Adv. Mater. 22 (2010) 853–857, https://doi.org/10.1002/adma.200903765.
[29] B.P. Chaplin, Critical review of electrochemical advanced oxidation processes for water treatment applications, Environ Sci Process Impacts 16 (2014) 1182–1203, https://doi.org/10.1039/C3EM00679D.
[30] H.S. Fogler, Essentials of Chemical Reaction Engineering, 5th Edition ed., Prentice Hall, Pearson Education, Inc., Boston, United State, 2016.
[31] J.-H. Chen, W.-T. Li, K.-Y. Cai, H.-J. Tu, Z.-T. Long, S. Akhtar, L.-D. Liu, Proton-coupled electron transfer controls peroxide activation initiated by a solid-water interface, Nat. Commun. 16 (2025) 3789, https://doi.org/10.1038/s41467-025-58917-w.
[32] H. Feng, Y. Han, Y. Wang, D.-F. Chai, J. Ran, W. Zhang, Z. Zhang, G. Dong, M. Qi, D. Guo, Advancing overall water splitting via phase-engineered amorphous/crystalline interface: a novel strategy to accelerate proton-coupled electron transfer, J. Colloid Interface Sci. 667 (2024) 237–248, https://doi.org/10.1016/j.jcis.2024.04.085.
[33] F. Zhu, W. Zhang, J. Xun, B.-J. Geng, Q.-M. Liang, Y. Yang, Proton donor/acceptor effects on electrochemical proton-coupled electron transfer reactions at solid–liquid interfaces, Curr. Opin. Electrochem. 42 (2023) 101377, https://doi.org/10.1016/j.coelec.2023.101377.
[34] J. He, Y. Zhao, Y. Li, Q. Yuan, Y. Wu, K. Wang, K. Sun, J. Wu, J. Jiang, B. Zhang, L. Wang, M. Fan, Joule heating-driven sp2-C domains modulation in biomass carbon for high-performance bifunctional oxygen Electrocatalysis, Nano Micro Lett. 17 (2025) 221, https://doi.org/10.1007/s40820-025-01725-0.
[35] C. Yang, F. Sun, Y. Zhang, Z. Qu, J. Zuo, W. Zhou, J. Gao, S. Liu, Y. Lu, Unveiling the coupling effect of sp2 domain size and local active sites in switching the selectivity of nanocarbon catalysts toward the oxygen electro-reduction, Nat. Commun. 16 (2025) 11270, https://doi.org/10.1038/s41467-025-66161-5.
[36] S. Chen, K. Huang, H.-F. Wang, H. Wang, H. Yu, J. Huang, Y. Cao, Electric-field enhanced three-dimensional flexible carbon felt as a host for Pt^{4+} ions extraction, Chem. Eng. J. 490 (2024) 151835, https://doi.org/10.1016/j.cej.2024.151835.
[37] J. Yang, X. Huang, J. Huang, H.-F. Wang, H. Wang, H. Yu, Y. Cao, Tailoring N/O functionalities on porous carbons for high-efficiency CO_2 cycloaddition: mechanistic insights and kinetic modeling, Chem. Eng. Sci. 320 (2026) 122490, https://doi.org/10.1016/j.ces.2025.122490.
[38] J. Huang, Y. Li, Y. Cao, F. Peng, Y. Cao, Q. Shao, H. Liu, Z. Guo, Hexavalent chromium removal over magnetic carbon nanoadsorbents: synergistic effect of fluorine and nitrogen co-doping, J. Mater. Chem. A 6 (2018) 13062–13074, https://doi.org/10.1039/c8ta02861c.
[39] E. Sun, J. Zou, B. Zhao, W. Zhou, Y. Sun, Y. Ding, Y. Li, M. Wang, M. Wu, Designing molecularly engineered proton highways via carboxyl-mediated hydrogen-bond networks in fuel cell catalyst layers, Chem. Eng. Sci. 332 (2026) 124095, https://doi.org/10.1016/j.ces.2026.124095.
[40] Y. Fan, M. Xu, Q. Li, M. Liu, X. Zhang, P. Chu, B. Zhang, H. Zhou, Y. Zhao, C. Liu, Carboxyl-CNTs act as “defensive shield” to boost proton insertion for stable and fast-charging aqueous Zn-Mn batteries, Small 21 (2025) 2501454, https://doi.org/10.1002/smll.202501454.
[41] A.A. Moya, Low-frequency approximations to the finite-length Warburg diffusion impedance: the reflexive case, J. Energy Storage 97 (2024) 112911, https://doi.org/10.1016/j.est.2024.112911.
[42] Y. Zhu, Y. Hao, T. Wang, F. Pan, H. Yu, J. Niu, Unveiling the fluid dynamics and mass transfer processes in a spatially confined flow-through electrochemical reactor, J. Environ. Sci. 160 (2026) 528–536, https://doi.org/10.1016/j.jes.2025.03.072.
[43] Y. Cheng, H. Wang, T. Qian, C. Yan, Interfacial engineering of carbon-based materials for efficient electrocatalysis: recent advances and future, EnergyChem 4 (2022) 100074, https://doi.org/10.1016/j.enchem.2022.100074.
[44] H. Xu, M. Ni, Chapter 4 - numerical simulation of hybrid systems based on solid oxide fuel cells, in: A. Berrada, R. El Mrabet (Eds.), Hybrid Energy System Models, Academic Press, 2021, pp. 91–127.
[45] J.-L. Burgot, Debye–Hückel Theory, in: J.-L. Burgot (Ed.), The Notion of Activity in Chemistry, Springer International Publishing, Cham, 2017, pp. 479–506.
[46] Y. Cao, J. Huang, Y. Li, S. Qiu, J. Liu, A. Khasanov, M.A. Khan, D.P. Young, F. Peng, D. Cao, X. Peng, K. Hong, Z. Guo, One-pot melamine derived nitrogen doped magnetic carbon nanoadsorbents with enhanced chromium removal, Carbon 109 (2016) 640–649, https://doi.org/10.1016/j.carbon.2016.08.035.
[47] Y. Cao, J. Huang, X. Peng, D. Cao, A. Galaska, S. Qiu, J. Liu, M.A. Khan, D. P. Young, J.E. Ryu, H. Feng, N. Yerra, Z. Guo, Poly(vinylidene fluoride) derived fluorine-doped magnetic carbon nanoadsorbents for enhanced chromium removal, Carbon 115 (2017) 503–514, https://doi.org/10.1016/j.carbon.2017.01.033.
[48] W. Chen, K. Wang, X. He, X. Chen, T. Huang, J. Chen, W. Huang, X. Yang, X. Ren, X. Ouyang, J. Liu, F. Pan, B. Xiao, Q. Zhang, J. Hu, Mitigating electrode polarization through electrolyte concentration optimization, Nano Energy 139 (2025) 110950, https://doi.org/10.1016/j.nanoen.2025.110950.
[49] S. Ahmed, N.G. N, M. Srivastava, M.D. Bouguern, A.K. M R, T.M.G. Selva, J.I. G. Dawkins, M.V.V. Reddy, M. Brassard, K. Zaghib, Electrode balancing as a key factor in lithium-ion batteries: from fundamentals to ultrafast charging, J. Power Sources 667 (2026) 239188, https://doi.org/10.1016/j.jpowsour.2025.239188.
[50] M.A. El Nemr, H.S. Jahin, M.H.H. Abbas, M.A. Hassaan, M.N.M. Ismail, A.E. Nemr, Adsorptive removal of Cr(VI) ions using nitrogen-doping activated carbon: influence of pH, kinetics, isotherm models, optimization, and efficiency evaluation, Sci. Rep. 16 (2026) 18187, https://doi.org/10.1038/s41598-026-53699-7.
[51] S. Singh, A.G. Anil, B. Uppara, S.K. Behera, B. Nath, P. N, S. Bhati, J. Singh, N. A. Khan, P.C. Ramamurthy, Adsorption and DFT investigations of Cr(VI) removal using nanocrystals decorated with graphene oxide, NPJ Clean Water 7 (2024) 17, https://doi.org/10.1038/s41545-024-00306-9.
[52] S. Yoon, S. Bae, Mechanistic study of Cr(VI) reduction by functionalized biochar: distinct roles of persistent free radicals, ascorbate moieties, and oxygen functional groups, Chem. Eng. J. 524 (2025) 169587, https://doi.org/10.1016/j.cej.2025.169587.
[53] F. Calle-Vallejo, Mainstream and Sidestream modeling in oxygen evolution Electrocatalysis, Acc. Chem. Res. 58 (2025) 2749–2759, https://doi.org/10.1021/acs.accounts.5c00439.
[54] T. Ashraf, B.T. Mei, G. Mul, Electrochemical decarboxylative oxidation of carboxylic acid mixtures on boron doped diamond electrodes, Electrochim. Acta 522 (2025) 145826, https://doi.org/10.1016/j.electacta.2025.145826.